WESTERN caspian UNIVERSITY

e-ISSN 3105-4293
p-ISSN 3105-4285

Journal of Nanotechnology and Innovative Materials

Vol 1, № 1, 2025

Baku - 2025

Western Caspian University

e-ISSN 3105-4293

p-ISSN 3105-4285

Journal of Nanotechnology and Innovative Materials

Vol 1, No 1
2025

DOI:10.54414/VWTT8467

www.https://jnim.wcu.edu.az

CONTENTS

http://doi.org/10.54414/EJJY5861

Research Article

Investigation into the Influence of Substitutions on the Structural Characteristics of Sr_2FeMoO_6

Vugar H. Mirzayev[1] and Dilmurod A. Rakhmanov[2]

[1]National University of Uzbekistan named after Mirzo Ulugbek, 20 Yangi Almazar Street, 100057 Tashkent, Uzbekistan
[2]Institute of Semiconductor Physics and Microelectronics, National University of Uzbekistan, 20 Yangi Almazar Street, 100057 Tashkent, Uzbekistan

Received: 05.11.2025 Accepted: 09.11.2025 Published: 19.11.2025

https://doi.org/10.54414/XVZB1367

Abstract

Sr_2FeMoO_6 is a half-metallic ferromagnet with a high Curie temperature, which positions it as a strong candidate for spintronic devices. Its lattice features ordered Fe and Mo cations on the B sites, and this arrangement underpins distinctive electronic transport and robust magnetic exchange. Here we examine Sr_2FeMoO_6 and the substituted phases $Sr_2FeMo_{1-x}Ta_xO_6$ with x = 0.05 and $Sr_2FeMo_{1-x}V_xO_6$ with x = 0.15 by neutron diffraction across multiple temperatures. The data show that temperature and B-site substitution drive measurable changes in unit-cell metrics and anisotropy. These results clarify the structural and thermal responses of this double perovskite family and inform their use in technology.

Keywords: neutron diffraction, rietveld refinement, substitutions, low temperature

1. Introduction

Sr_2FeMoO_6 is a double perovskite oxide that exhibits half-metallic ferromagnetism together with a high Curie temperature, which makes it a strong candidate for spintronic devices. Its lattice hosts an ordered arrangement of Fe and Mo cations on the B sites, and this chemical ordering drives unusual electronic transport and robust magnetic exchange. As a result, the material combines near-perfect spin polarization with stable long-range magnetism at technologically relevant temperatures [1]. Furthermore, Sr_2FeMoO_6 has been explored for applications in solid oxide fuel cells due to its strong electronic conductivity and thermal resilience [2].

Sr_2FeMoO_6 is a B-site-ordered double perovskite that combines highly spin-polarized conduction with stable ferrimagnetic behavior at and above room temperature. Its magnetic and electronic performance originates from the distinctive interaction between Fe and Mo ions and the resulting band structure [3]. Achieving high magnetization, strong spin polarization, and reliable transport properties depends on strict control of composition, oxygen non-stoichiometry, and cation ordering in both bulk samples and thin film architectures [4]. Because its defect chemistry can be adjusted over a wide range, Sr_2FeMoO_6 serves as a flexible material platform for spintronic elements and magnetoresistive devices used in oxide-based electronics [5]. Tailored microstructures and composite configurations also produce strong responses in the radio frequency and microwave regimes, which makes the material useful for sensing technologies and electromagnetic interference management [6]. In addition to these functions, the combined electrical conductivity, redox durability, and ability to accommodate dopants make Sr_2FeMoO_6 a promising option for electrocatalytic applications and as an anode material in solid oxide electrochemical systems [1].

Sr_2FeMoO_6 is a B-site ordered double perovskite that shows half-metallicity and robust ferrimagnetism near room temperature. Large low-field magnetoresistance arises from spin-polarized tunneling across grain

boundaries. This result established SFMO as a model oxide for spintronics [7]. Neutron diffraction and magnetometry confirm ferrimagnetic ordering arising from Fe^{3+}–O–Mo^{5+} pathways in ordered SFMO and reveal how even modest Fe/Mo antisite disorder measurably depresses the refined magnetic moments and transition temperature [8]. Room-temperature neutron data on SFMO–δ ceramics underscore that oxygen-defect chemistry subtly distorts the cell and modulates ordered moments, reinforcing the tight coupling among oxygen content, structural metrics, and ferri-magnetic order [9].

The study [10] revealed that increasing the total sintering time significantly improved Fe/Mo cation ordering in Sr_2FeMoO_6, reducing antisite defects and increasing the degree of ordering from 44.9% to 80.2%. Rietveld refinement showed a gradual decrease in unit cell volume and bond lengths (Fe–O and Mo–O) with extended sintering, indicating a more compact and ordered crystal structure. Additionally, the Fe–O1–Mo bond angle increased with sintering time, reflecting reduced octahedral tilting and enhanced linearity along the Fe–O–Mo chains. A structural phase transition from cubic ($Fm\bar{3}m$) to tetragonal ($I4/m$) symmetry occurs in Sr_2FeMoO_6 near 400 K, accompanied by octahedral rotations and the onset of ferrimagnetic ordering. Neutron diffraction and Mössbauer spectroscopy revealed a saturated Fe magnetic moment of ~4.3 μB and an intermediate Fe valence state, with approximately 6% Mo-site vacancies contributing to local structural and magnetic inhomogeneity [11]. Cation ordering in the $I4/m$ structure and antisite defects control the balance between high saturation magnetization, metallic transport, and spin polarization. Targeted A- or B-site substitutions and careful oxygen control tune the Curie temperature and magnetoresistance. This review frames the structure–property rules that guide later work [12]. Systematic neutron refinements of $Sr_2Fe_{0.75}T_{0.25}MoO_6$ (T = Cr, Mn, Co, Ni) demonstrate dopant-specific lattice distortions and disorder that degrade M_s and metallicity to differing degrees, mapping how 3d-dopant chemistry perturbs Fe–O–Mo exchange [13]. In $Sr_2Fe_{1-x}Cr_xMoO_{6-\gamma}$, increasing Cr systematically reduces M_s and increases resistivity by disrupting Fe–O–Mo double-exchange and promoting antisites/oxygen defects, providing a clear, composition-dependent picture of structure–magnetism coupling [14].

Magnetocaloric measurements on SFMO and W-doped analogs link structural distortions to the magnetic-entropy change, indicating that judicious B-site chemistry can shift operating windows toward technologically relevant temperatures [15].

In this context, our research focuses on further understanding the structural behavior of Sr_2FeMoO_6-based systems under different doping strategies and temperature conditions using high-resolution neutron diffraction and Rietveld analysis.

2. Research Method

Neutron diffraction measurements were conducted over a range of temperatures using the High-Resolution Fourier Diffractometer (HRFD) at the Frank Laboratory of Neutron Physics, Joint Institute for Nuclear Research (JINR), Dubna, Russia. The instrument provides high angular resolution and is optimized for the precise determination of lattice parameters and atomic positions, allowing accurate tracking of temperature-induced structural variations in the studied samples [16]. The purpose was to investigate the structural behavior of the parent compound Sr_2FeMoO_6 and its cation-substituted derivatives, namely $Sr_2FeMo_{1-x}Ta_xO_6$ (x = 0.05) and $Sr_2FeMo_{1-x}V_xO_6$ (x = 0.15). Samples were synthesized with controlled stoichiometry and uniform microstructure to ensure reliable diffraction data. Temperature and B-site substitution with Ta and V were varied systematically to assess their impact on unit-cell metrics. Lattice parameters were obtained by full-profile Rietveld refinement, which also yielded fit statistics and peak-broadening indicators. These measurements provide a consistent basis for interpreting thermal and substitution effects in this double perovskite system [17,18].

3. Results and Discussion

Neutron diffraction experiments were conducted on Sr_2FeMoO_6-based samples at varying dopant concentrations and temperatures. The diffraction spectra were refined using the Rietveld method implemented in the FullProf Suite software [19,20].

In the initial undoped state, the diffraction pattern illustrates a well-defined structure, from which changes in lattice parameters with temperature were identified (Figure 1).

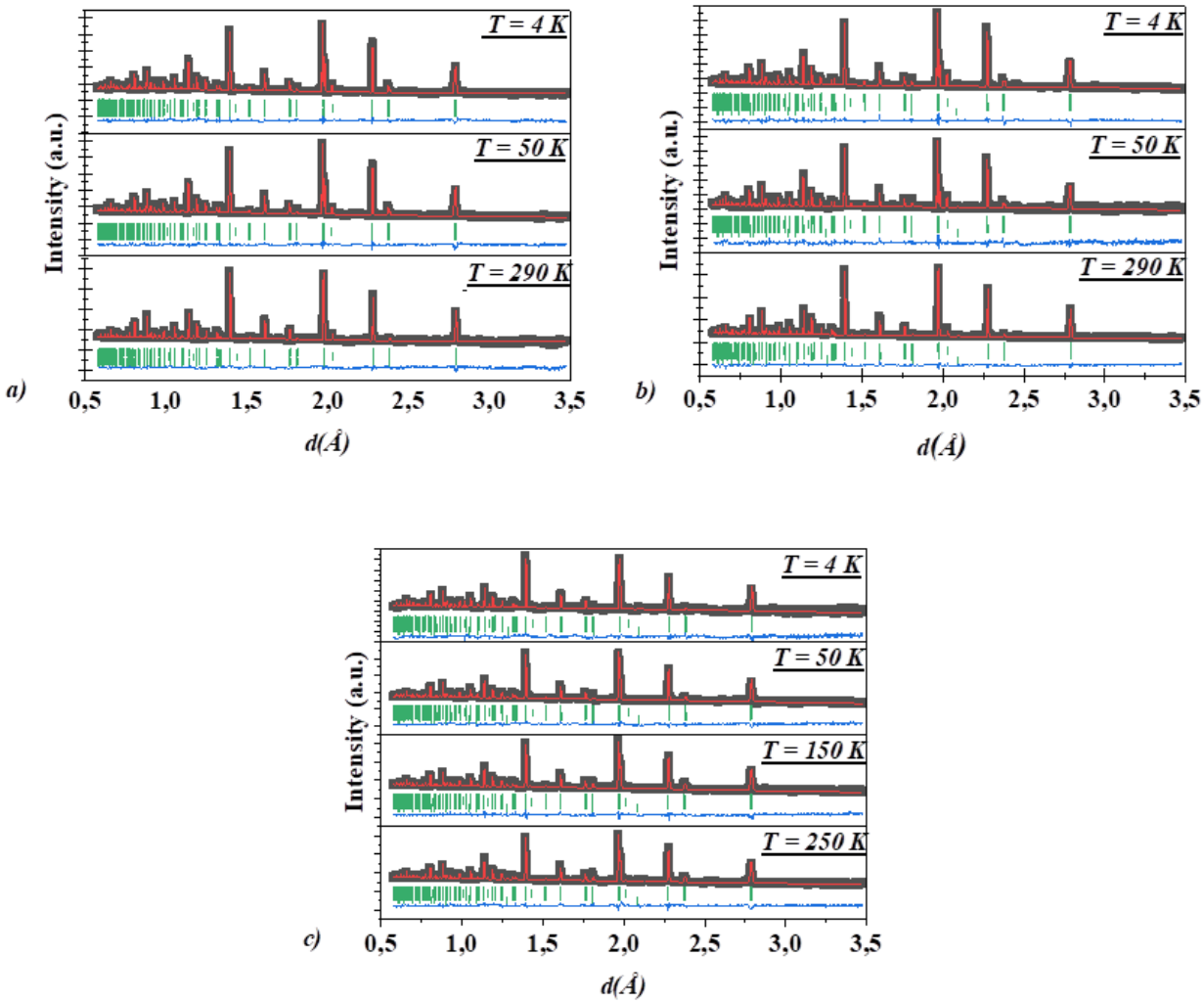

Figure 1. Neutron diffraction patterns of (a) initial **Sr_2FeMoO_6,** (b) **$Sr_2FeMo_{1-x}V_xO_6$** (x = 0.15), and (c) **$Sr_2FeMo_{1-x}Ta_xO_6$** (x = 0.05) at different temperatures. Black dots represent experimental data, the red line is the Rietveld refinement fit, green vertical ticks indicate Bragg reflection positions, and the blue line shows the difference between observed and calculated intensities.

Following V doping at x = 0.15, diffraction patterns were collected at three temperatures, as shown in Fig. 1b. In addition to the perovskite reflections, weak extra peaks appear that do not index to the Sr_2FeMoO_6 cell and are assigned to aluminum and copper from the sample environment used to secure the containers under the measurement conditions. In the Ta doped compound $Sr_2FeMo_{1-x}Ta_xO_6$ with x = 0.05, the unit cell volume remains close to that of the undoped sample, with a slight increase at intermediate temperature and reaching 245.95 Å^3 at 250 K as shown in Fig. 1c. The a axis shows a minor expansion while the c axis is nearly temperature independent, which indicates that the framework is largely preserved with Ta substitution. The full set of refined structural parameters is summarized in Table 1. For the undoped Sr_2FeMoO_6, the unit cell volume increases with temperature from 244.63 Å^3 at 4 K to 246.14 Å^3 at 290 K, consistent with moderate thermal expansion.

For the V-doped composition $Sr_2FeMo_{1-x}V_xO_6$ with x equal to 0.15, the unit cell volume remains smaller at all temperatures when compared with the undoped material and the Ta-substituted sample [21]. At 4 K, the volume reaches its lowest value of 243.99 Å^3. The c-axis shows the strongest decrease, which indicates that the

introduction of vanadium produces a clear lattice contraction. This shrinkage is more evident than the effect produced by Ta substitution and demonstrates the stronger structural impact of vanadium on the Sr_2FeMoO_6 lattice.

Table 1. The changes in structural parameters after substitution.

Space group I 4/m m m	a	c	V
Sr_2FeMoO_6 T = 4 K	5.5599(1)	7.9134(1)	244.627(6)
Sr_2FeMoO_6 T = 50 K	5.5607(1)	7.9138(2)	244.71(1)
Sr_2FeMoO_6 T = 290 K	5.5785(1)	7.9096(2)	246.14(1)
$Sr_2FeMo_{1-x}V_xO_6$ x=0.15, T = 4 K	5.5560(1)	7.9040 (2)	243.994 (1)
$Sr_2FeMo_{1-x}V_xO_6$ x=0.15, T = 50 K	5.5547(1)	7.9039(2)	243.98(1)
$Sr_2FeMo_{1-x}V_xO_6$ x=0.15, T = 290 K	5.5730(1)	7.8986(2)	245.32(1)
$Sr_2FeMo_{1-x}T_{ax}O_6$ x=0.05, T = 4 K	5.5628 (2)	7.9059(2)	244.778(2)
$Sr_2FeMo_{1-x}Ta_xO_6$ x=0.05, T = 50 K	5.5628(2)	7.9101(3)	244.78(1)
$Sr_2FeMo_{1-x}Ta_xO_6$ x=0.05, T = 150 K	5.5676 (2)	7.9085 (3)	245.15(2)
$Sr_2FeMo_{1-x}TaxO_6$ x=0.05, T = 250 K	5.576(1)	7.909(1)	245.95(5)

These findings emphasize the role of B-site substitution in tuning the thermal and structural behavior of double perovskites. While Ta maintains structural integrity across temperature ranges, V leads to distinct lattice shrinkage, underlining the importance of dopant selection for potential applications where thermal and structural stability are critical.

4. Conclusion

Taken together, the results show that temperature and B-site substitution strongly govern the crystal structure of Sr_2FeMoO_6. Thermal expansion increases the unit-cell volume of the pristine compound, and the effect is anisotropic along the a and c axes. Ta incorporation keeps the lattice essentially unchanged and points to good structural robustness under heating. V substitution produces a clear lattice contraction, most notably along the c axis, consistent with a modified bonding environment and altered octahedral distortions. These insights identify B-site chemistry as an effective handle to tailor thermal and structural responses in double perovskites, and they guide optimization for spintronic and solid-oxide energy applications.

Author Contributions

Dilmurod A. Rakhmanov: conceptualization methodology, writing original draft.

Vugar H. Mirzayev: conceptualization, funding, acquisition, project administration.

Funding

No funding was received for this research.

Conflicts of Interest

The authors declare that they have no conflicts of interest.

Supplementary Information

Not applicable.

Ethical Approval

Not applicable.

Acknowledgments

The authors thank A.S. Abiyev for his assistance in conducting the experiment.

Data and Code Availability

The data supporting the findings of this study are available from the corresponding author upon reasonable request. No custom code was used in this study.

Abbreviations

Strontium Iron Molybdate (Sr_2FeMoO_6), Iron (Fe), Molybdenum (Mo), Strontium Iron Molybdenum Tantalum Oxide ($Sr_2FeMo_{1-x}Ta_xO_6$), Strontium Iron Molybdenum Vanadium Oxide ($Sr_2FeMo_{1-x}V_xO_6$), SFMO (Sr_2FeMoO_6), Chromium (Cr), Manganese (Mn), Cobalt (Co), Nickel (Ni), Saturation Magnetization (M_s) High Resolution Fourier Diffractometer (HRFD), Joint Institute for Nuclear Research (JINR).

References

1. Liao, Y., Xi, X., Chen, H., Liu, J., Fu, X. Z., & Luo, J. L. (2024). The emerging Sr2FeMoO6-based electrocatalysts for solid oxide electrochemical cell: synthesis, modulation and applications. https://doi.org/10.20517/cs.2023.47
2. Suchaneck, G., Kalanda, N., Yarmolich, M., Artiukh, E., Gerlach, G., & Sobolev, N. A. (2022). Magnetization of magnetically inhomogeneous Sr2FeMoO6-δ nanoparticles. *Electronic Materials*, *3*(1), 82-92. https://doi.org/10.29003/m3067.mmmsec-2022/58-58
3. Sarma, D. D., Mahadevan, P., Saha-Dasgupta, T., Ray, S., & Kumar, A. (2000). Electronic Structure of Sr 2 FeMoO 6. *Physical review letters*, *85*(12), 2549. https://doi.org/10.1103/physrevlett.85.2549
4. Hauser, A. J., Williams, R. E., Ricciardo, R. A., Genc, A., Dixit, M., Lucy, J. M., & Yang, F. (2011). Unlocking the potential of half-metallic Sr 2 FeMoO 6 films through controlled stoichiometry and double-perovskite ordering. *Physical Review B—Condensed Matter and Materials Physics*, *83*(1), 014407. https://doi.org/10.1103/physrevb.83.014407
5. Sarma, D. D. (2001). A new class of magnetic materials: Sr2FeMoO6 and related compounds. *Current Opinion in Solid State and Materials Science*, *5*(4), 261-268. https://doi.org/10.1016/s1359-0286(01)00014-6
6. Das, R., Chaudhuri, U., & Mahendiran, R. (2021). Microwave magnetoresistance and microwave absorption in Sr2FeMoO6. *ACS Applied Electronic Materials*, *3*(7), 3072-3078. https://doi.org/10.1021/acsaelm.1c00304
7. Kobayashi, K. I., Kimura, T., Sawada, H., Terakura, K., & Tokura, Y. (1998). Room-temperature magnetoresistance in an oxide material with an ordered double-perovskite structure. *Nature*, *395*(6703), 677-680. https://doi.org/10.1038/27167
8. Chung, M. K., Huang, P. J., Li, W. H., Yang, C. C., Chan, T. S., Liu, R. S., & Lynn, J. W. (2006). Crystalline and magnetic structures of Sr2FeMoO6 double perovskites. *Physica B: Condensed Matter*, *385*, 418-420. https://doi.org/10.1016/j.physb.2006.05.140
9. Sikolenko, V., Kalanda, N., Yarmolich, M., Petrov, A., Karpinsky, D., Efimov, V., & Savvin, S. (2025). Neutron Diffraction Study of the Magnetic Structure of Sr2FeMoO6–δ. *Physics of Particles and Nuclei Letters*, *22*(5), 1278-1282. https://doi.org/10.1134/s1547477125701559
10. Hu, Y. C., Ge, J. J., Ji, Q., Lv, B., Wu, X. S., & Cheng, G. F. (2010). Synthesis and crystal structure of double-perovskite compound Sr2FeMoO6. *Powder Diffraction*, *25*(S1), S17-S21. https://doi.org/10.1154/1.3478711
11. Chmaissem, O., Kruk, R., Dabrowski, B., Brown, D. E., Xiong, X., Kolesnik, S., & Kimball, C. W. (2000). Structural phase transition and the electronic and magnetic properties of Sr 2 FeMoO 6. *Physical Review B*, *62*(21), 14197. https://doi.org/10.1103/physrevb.62.14197

12. Serrate, D., De Teresa, J. M., & Ibarra, M. R. (2006). Double perovskites with ferromagnetism above room temperature. *Journal of Physics: Condensed Matter*, *19*(2), 023201. https://doi.org/10.1088/0953-8984/19/2/023201
13. Ritter, C., Blasco, J., De Teresa, J. M., Serrate, D., Morellon, L., Garcia, J., & Ibarra, M. R. (2004). Structural and magnetic details of 3d-element doped Sr2Fe0. 75T0. 25MoO6. *Solid state sciences*, *6*(5), 419-431. https://doi.org/10.1016/j.solidstatesciences.2004.02.007
14. Blasco, J., Ritter, C., Morellon, L., Algarabel, P. A., De Teresa, J. M., Serrate, D., & Ibarra, M. R. (2002). Structural, magnetic and transport properties of Sr2Fe1− xCrxMoO6− y. *Solid state sciences*, *4*(5), 651-660. https://doi.org/10.1016/s1293-2558(02)01309-2
15. Zhong, W., Liu, W., Wu, X. L., Tang, N. J., Chen, W., Au, C. T., & Du, Y. W. (2004). Magnetocaloric effect in the ordered double perovskite Sr2FeMo1− xWxO6. *Solid state communications*, *132*(3-4), 157-162. https://doi.org/10.1016/j.ssc.2004.07.060
16. Hasanov, K. M., Abiyev, A. S., Sumnikov, S. V., Kostishyn, V. G., Trukhanov, A. V., Trukhanov, S. V., & Turchenko, V. A. (2025). Effects of Non-Isovalent Substitution on the Structural and Magnetic Properties of SrFe12-x (CoSn) xO19 Solid Solutions (x= 0–0.5). *Journal of Alloys and Compounds*, 182512. https://doi.org/10.1016/j.jallcom.2025.182512
17. Abiyev, A. S., Samadov, S. F., Mehdiyeva, R. N., Dadashzade, G. A., Kvasovich, E. O., & Huseynov, E. M. (2025). Oxidation dynamics in gamma-irradiated TiN nanoparticles after annealing. *Ceramics International*. https://doi.org/10.1016/j.ceramint.2025.04.019
18. Abiyev, A. S. (2021). Physicochemical processes in aluminum nanoparticles at high temperatures. *Advanced Physical Research*, *3*(3), 137-141. https://doi.org/10.4028/www.scientific.net/amr.872.248
19. Samadov, S. F., Samedov, O. A., Mirzayeva, D. M., Nguyen, H. H. A., & Mirzayev, M. N. (2025). Effect of gamma irradiation and thermal annealing on defect formation in ZrB2 nanocrystals. *Physica B: Condensed Matter*, 417807. https://doi.org/10.1016/j.physb.2025.417807
20. Samadov, S. F., Abiyev, A. S., Asadov, A. G., Trung, N. V. M., Sidorin, A. A., Samedov, O. A., & Mirzayev, M. N. (2024). Investigating the crystal structure of ZrB2 under varied conditions of temperature, pressure, and swift heavy ion irradiation. *Ceramics International*, *50*(2), 3727-3732. https://doi.org/10.1016/j.ceramint.2023.11.125
21. Abdullayev, A. P., Samadov, S. F., Abiyev, A. S., Sidorin, A. A., Trung, N. V. M., Orlov, O. S., & Musazade, I. V. (2025). Defect and crystal structure variation in Tl-doped TlGaTe2 semiconductor alloys: An experimental and theoretical study. *Journal of Alloys and Compounds*, *1038*, 182773. https://doi.org/10.1016/j.jallcom.2025.182773

Research Article

Effect of Nickel-Chromium Alloy Additions and Regenerative Annealing on the Physicomechanical Properties of Cast Iron-Based Composites

Ilhama A. Hamdullayeva[1], Durdana F. Rustamova[2], and Madina F. Nabili[3]

[1]Institute of Physics, Ministry of Science and Education, 131 H. Javid Avenue, AZ1143 Baku, Azerbaijan
[2]Department of Mechanics and Mathematics, School of Advanced Technologies and Innovation Engineering, Western Caspian University, 17A Ahmad Rajabli Street, III Parallel, AZ1001 Baku, Azerbaijan
[3]First Chayli Secondary School named after Kamil Samadov, Ministry of Science and Education, First Chayli Village, Shamakhi District, AZ5600 Azerbaijan

Received: 05.11.2025 Accepted: 19.11.2025 Published:19.11.2025

https://doi.org/10.54414/RZZY2242

Abstract

This study examines the potential to enhance the physical and mechanical properties of cast-iron-based composite materials produced by regenerative melting of cast-iron shavings with a nickel-chromium alloy. Calculations show that carbon release intensifies with increased softening rates, accompanied by changes in the absolute mass of the scrap. However, temperatures above 1000°C are undesirable, as particle agglomeration occurs, creating additional processing challenges. Regenerative annealing of cast iron scrap improves its physical and technological characteristics. A notable increase in hardness was observed in "iron-cast iron" composite samples containing 3 % nickel-chromium alloy. In contrast, annealing the scrap at 700°C did not result in any significant improvement in sample strength.

Keywords: cast iron composite, regenerative melting, nickel-chromium alloy, cast iron scrap, annealing, hardness, carbon release, mechanical properties

1. Introduction

The physical and mechanical properties of cast iron can be significantly improved by incorporating various steel alloys, as demonstrated in numerous studies [1-3]. Cast iron alloys inherently possess high carbon-graphite content, which plays a critical role in their structural and mechanical behavior.

Cast iron scrap is commonly oxidized during mechanical processing, particularly in ball mills, where lubricating-cooling fluids promote oxidation. In this oxidized state, cast iron granules deform under cold working but do not readily sinter unless purer components are introduced into the mixture. When oxidized scrap is used as a non-carbonaceous (carbon-depleted) component, it decreases briquette strength and acts as a gas generator during sintering (heating). As a result, the desired physical and mechanical properties of the final alloy cannot be achieved [4].

To compensate for this, small amounts of pure cast iron are sometimes added to the charge, or the material is held at elevated temperatures for prolonged periods. However, both methods are inefficient and economically disadvantageous. Therefore, research aimed at developing cast iron composites with controllable carbon content is of high scientific and industrial relevance.

One promising approach involves regenerative annealing of cast iron scrap prior to its use. This treatment improves pressability and sinterability and enhances the overall structural quality of synthesized iron-cast iron-nickel–chromium alloys. During regenerative annealing, diffusion of alloying elements increases, their distribution throughout the volume becomes more uniform, and structural homogenization accelerates [5, 6]. Consequently, the kinetics of structure formation are strongly influenced by the transformation processes occurring throughout the material volume, including the reduction behavior of cast iron and other related physicochemical factors [7].

2. Research Method

Reductive regeneration was carried out on cast iron particulate with a particle size of 63-200 μm. The recovery temperature range was set between 700 and 1000°C. This interval was selected because regeneration efficiency decreases below 700°C, whereas temperatures above 1000°C cause partial sintering of iron particles, leading to agglomeration and requiring repeated grinding [8].

The carbonization behavior of the cast iron particulate was investigated using thermogravimetric analysis (TGA) on a Setaram instrument under an endogas atmosphere [9]. Samples were heated at a rate of 10°C/min to a maximum temperature of 1000°C. The evolution of CO and CO_2 gases during the process was quantified using a chromatographic analyzer.

3. Results and Discussion

The experimental results are presented in Figure 1. As shown, increasing the regeneration temperature from 700°C to 1000°C leads to a progressive increase in both the absolute mass loss of the particulate (Curve 1) and the rate of mass decrease (Curve 2).

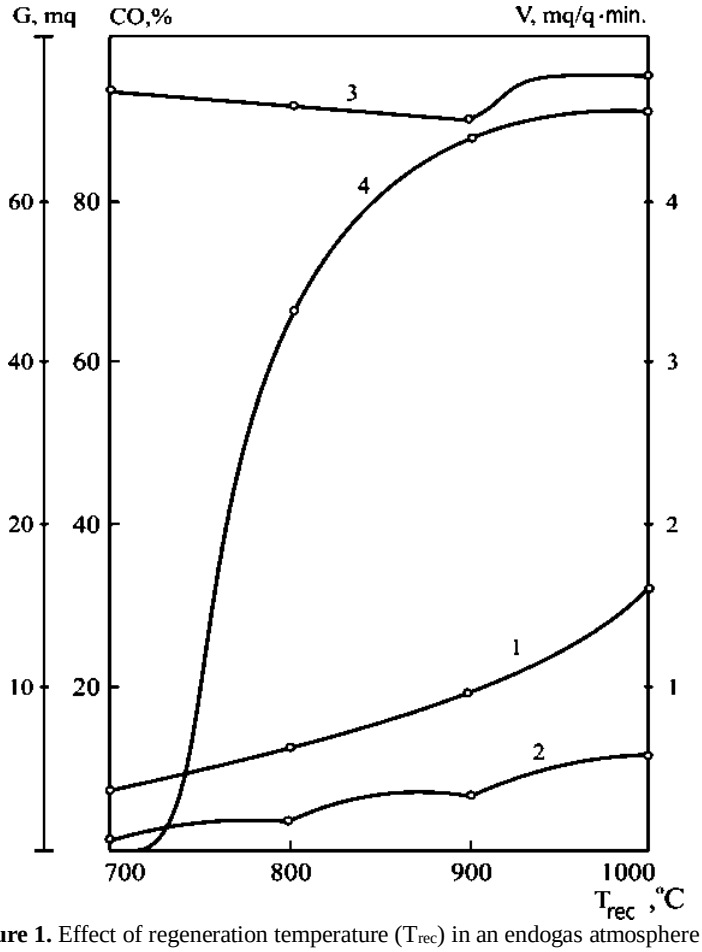

Figure 1. Effect of regeneration temperature (T_{rec}) in an endogas atmosphere on:

(1) Absolute mass decrease (G, mg), (2) Rate of mass decrease (V_{mass}, mg/g min), (3) CO concentration in the furnace gas (CO, %), and (4) CO formation rate due to Reactions (4) and (5) (V_{CO}, mg/g min).

3.1. Mechanism of Reductive Regeneration

The mechanism of regenerative hardening of cast iron particulate can be interpreted through the sequence of reactions occurring at the interface between the metal matrix and the oxide layer. The reduction of iron oxides by carbon proceeds through the following reactions:

Direct reactions with carbon:

$$[C] + Fe_xO_y \rightarrow Fe_xO_{y-1} + CO \quad (1)$$

$$C_{gr} + Fe_xO_y \rightarrow Fe_xO_{y-1} + CO \quad (2)$$

Gas–solid reduction:

$$Fe_xO_y + CO \rightarrow Fe_xO_{y-1} + CO_2 \quad (3)$$

The carbon monoxide (CO) formed in these reactions diffuses through the pores of the oxide scale and further participates in the reduction of higher oxides. The carbon dioxide (CO_2) produced can react with carbon at the metal–graphite interface [10]:

$$[C] + CO_2 = 2CO \quad (4)$$

$$C_{gr} + CO_2 = 2CO \quad (5)$$

According to Reference [11], carbonization of cast iron particulate in a CO_2 atmosphere proceeds effectively between 840-890°C. Therefore, in the range of 700-890°C, the decarbonization process is governed primarily by Reaction (1), since direct contact between graphite and the oxide scale is limited at these temperatures.

The observed increase in the CO formation rate, followed by its stabilization as the temperature rises from 700°C to 900°C (Figure 1, Curve 4), indicates that oxide reduction is relatively weak in this region and CO escapes easily from the particle interior. As a result, the concentration of CO in the furnace atmosphere remains nearly constant (Figure 1, Curve 3).

3.2. Microstructural Evolution of Cast Iron Particulate

As a consequence of carbonization and reduction, the slag-derived spongy particles develop an irregular, rough surface morphology (Figure 2a-c). Their surfaces and cores consist mainly of metal oxides together with significant quantities of non-metallic inclusions. After purification (Figure 2c), the microstructure of the cast iron particulate is characterized by a ferritic matrix with pores; oxide residues persist at locations formerly occupied by graphite. Similar features have been reported for regenerated cast iron briquettes [12, 13].

Figure 2 presents the microstructures of composite briquettes produced with and without inoculation and annealed at 1000°C. The iron-rich regions in the briquettes form compact ferritic structures, whereas cast-iron regions contain ferrite along with multiple inclusions and fine porosity, consistent with earlier observations [11].

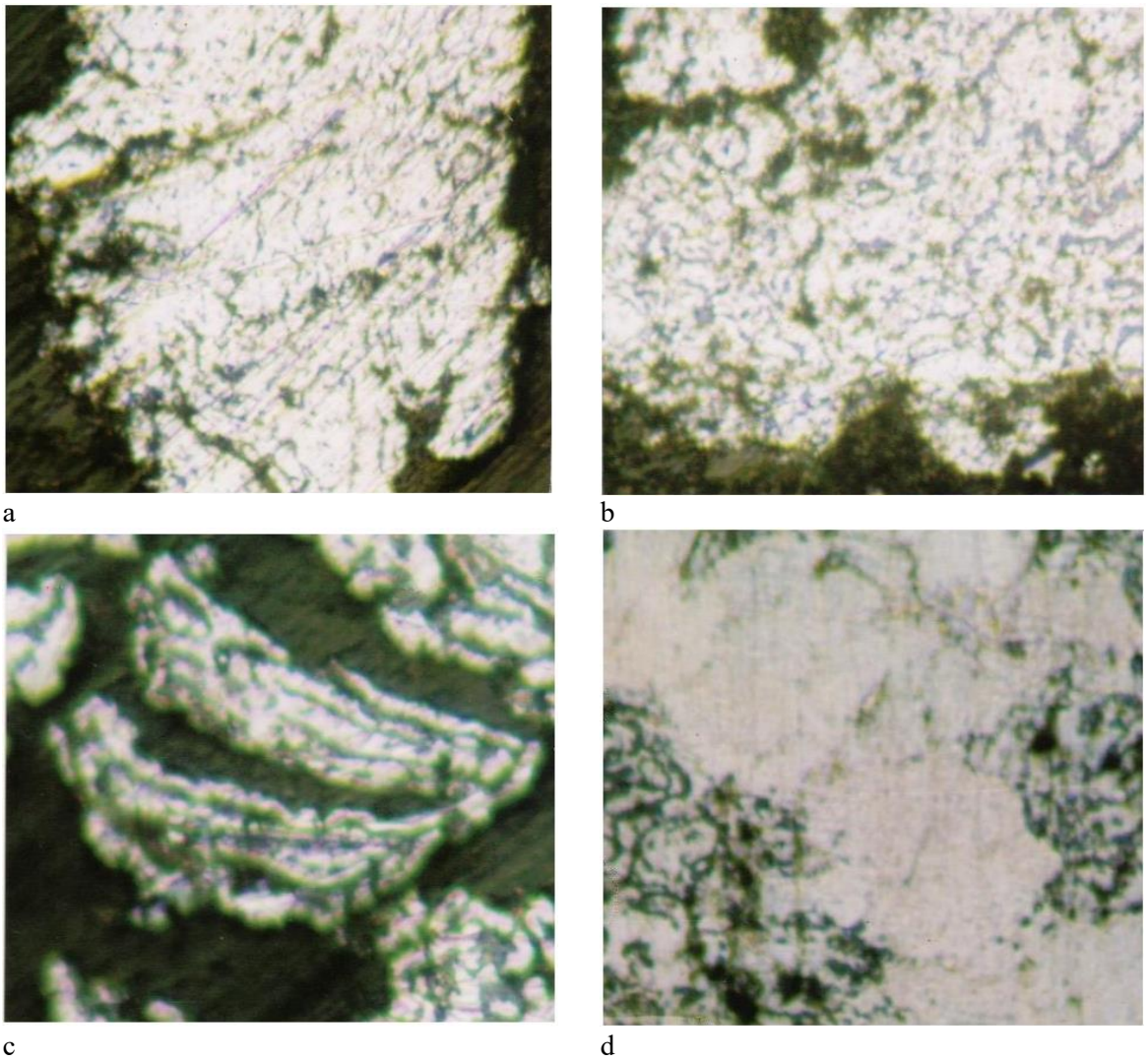

Figure 2. Microstructure (x 400) of cast iron particulate after reductive regeneration and composite briquettes (particle size: 63-200 μm; pressing pressure: 700 MPa). (a, b): Non-inoculated particulate after reductive regeneration. (c): Inoculated particulate after purification. (d): Microstructure of the 'iron-cast iron' composite briquette (inoculated).

3.3. Effect of Regeneration Temperature on Physical and Technological Properties

Figure 3 demonstrates that the density of the regenerated cast iron particulate increases with temperature (Curve 1), reaching 6.63 g/cm³ at 1000°C. Further studies revealed that briquettes pressed from the regenerated particulate exhibit an increased density of 5.4-5.5 g/cm³, indicating that reductive regeneration significantly enhances densification.

Porosity of the briquetted material (Curve 2) decreases with increasing regeneration temperature, reflecting improved structural compaction.

Flowability (Curve 3), expressed as flow time through a standard funnel, decreases as temperature increases. This decline corresponds to an increase in the specific surface area of the particulate, which enhances the reactivity and promotes regeneration.

In contrast, the tap density (Curve 4) initially increases, then stabilizes or slightly decreases, suggesting a complex relationship between particle surface modification and packing behavior.

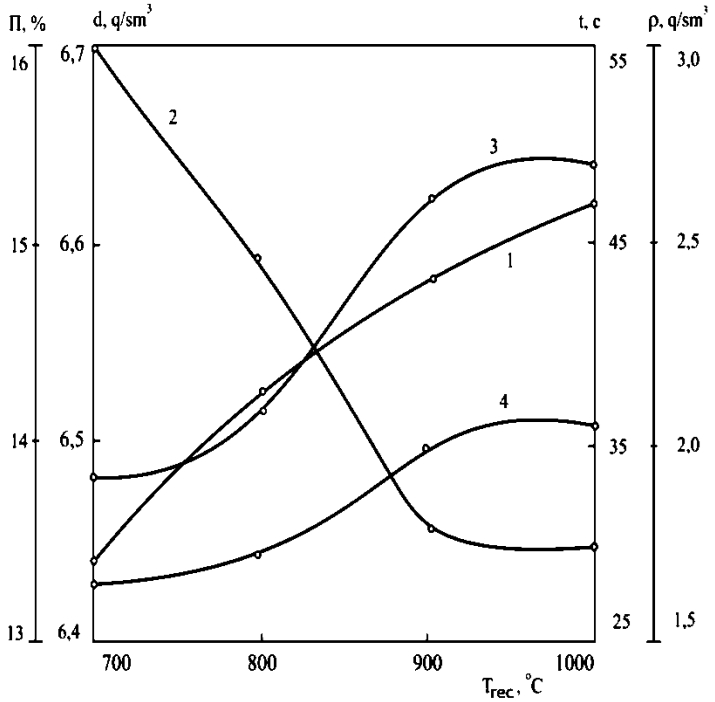

Figure 3. Effect of regeneration temperature ((T$_{rec}$, °C)) on physical and technological properties of cast iron particulate: (1) Density (d, g/cm^3), (2) Porosity (II, %), (3) Flowability (t, s), (4) Tap Density (ρ, g/cm^3).

Paradoxically, as the annealing temperature increases, the intensity of particulate regeneration also increases, leading to a noticeable decrease in foreign inclusions. However, particles that undergo stronger regeneration become denser and heavier compared to weakly regenerated ones. This behavior is reflected in the mechanical characteristics of the composite material sintered at 1100°C (Figure 4), where both tensile strength and hardness exhibit a dependence on the regeneration temperature.

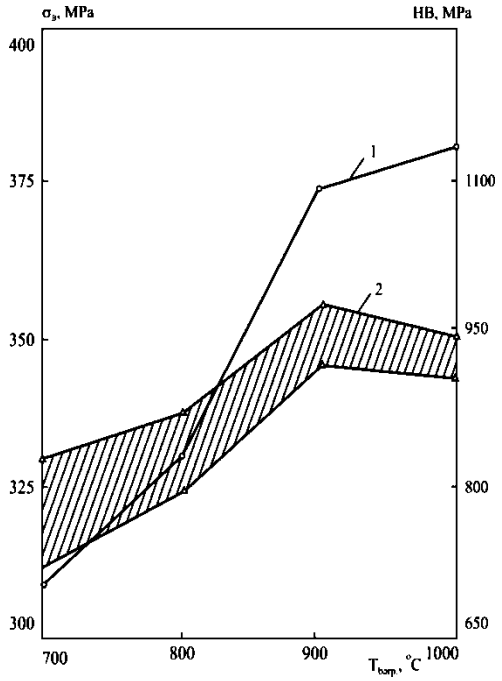

Figure 4. Dependence of the mechanical properties of the composite material (sintered at 1100°C) on the regeneration temperature (T$_{rec}$, °C): (1) Tensile strength (σ$_b$, MPa), (2) Hardness (HB, MPa).

4. Conclusion

This study demonstrates that increasing the annealing (softening) temperature accelerates carbon release and intensifies the reduction of iron oxides, resulting in a progressively greater mass loss of the cast iron particulate. However, temperatures above 1000°C are undesirable because they promote particle adhesion and partial sintering, which complicates further processing.

Annealing the cast iron particulate significantly improves its physical and technological properties relative to the untreated material. Enhanced wetting of the particulate by both iron and nickel-chromium alloys leads to improved diffusion of alloying elements into the composite structure. A well-defined diffusion zone is observed between the nickel-chromium alloy and the "iron-cast iron" composite when the particulate is annealed at 1000°C.

Mechanical testing reveals that composites produced with the "iron-cast iron" mixture and reinforced with 3% nickel-chromium (Ni-Cr) alloy exhibit superior tensile strengths. In contrast, particulate annealed at 700°C does not contribute to any improvement in mechanical performance, confirming that higher regeneration temperatures are necessary to achieve structural enhancement.

Overall, the study establishes that controlled reductive regeneration at optimal temperatures significantly enhances the microstructural integrity, densification behavior, and mechanical properties of cast iron particulate-based composites.

Author Contributions

All authors contributed to the conceptualization, methodology, data analysis, and writing of the manuscript.

Funding

This research received no external funding.

Conflict of Interest

The authors declare no conflicts of interest.

Acknowledgment

The authors express their sincere gratitude to Dr. Ilhama Hamdullayeva for her valuable guidance, constructive feedback, and continuous support throughout the preparation of this research.

Data Availability Statement

The authors declare that the data supporting the findings of this study are available within the article.

Abbreviations

Carbon Monoxide (CO), Carbon Dioxide (CO_2), Iron Oxide (Fe_xO_y), Graphite Carbon (C_{gr}), Recovery Temperature (T_{rec}), Thermogravimetry (TG), Nickel-Chromium (Ni-Cr), Brinell Hardness (HB), Micrometer (μm).

References

1. NIINTI. (1977). Powder metallurgy abroad (signal information on firm documentation) (Issues 1–2). Kyiv, Ukraine: NIINTI.
2. Kubo, O., Ishibashi, S., Koie, T., Matsubara, Y., & Kishitake, K. (2005). Effect of chemical composition on microstructure and characteristics of high chromium Ni-hard cast iron. Journal of Japan Foundry Engineering Society, 77(5), 293-300. https://doi.org/10.11279/jfes.77.293

3. Królczyk, G., Feldshtein, E., Dyachkova, L., Michalski, M., Baranowski, T., & Chudy, R. (2020). On the microstructure, strength, fracture, and tribological properties of iron-based MMCs with addition of Mixed Carbide Nanoparticulates. Materials, 13(13), 2892. https://doi.org/10.3390/ma13132892
4. Liu, T., Sun, J., Xiao, Z., He, J., Shi, W., & Cui, C. (2023). Effect of multi-element microalloying on the structure and properties of high chromium cast iron. Materials, 16(9), 3292. https://doi.org/10.3390/ma16093292
5. Radomyselskiy, I. D., & Kuzenkova, M. A. (1961). Investigation of properties of structural metal-ceramic materials made from mixtures of iron and cast iron powders. Powder Metallurgy, (4), 56–62.
6. Issagulov, A. Z., Kvon, S. S., Kulikov, V. Y., Aubakirov, D. R., & Chsherbakova, Y. P. (2023). Studying the chrome-nickel cast iron structure and properties after modification on industrial samples. Metalurgija, 62(1), 122-124.
7. German, R. M. (1998). Powder metallurgy of iron and steel. (No Title). https://doi.org/10.5860/choice.36-0981
8. Wunderlich, B. (2005). Thermal analysis of polymeric materials. Berlin, Heidelberg: Springer Berlin Heidelberg.
9. Alghtani, A. H., Alsharef, M., & El-Aziz, K. A. (2022). Characterization of iron powder produced by reduction of hot-rolled mill scale in hydrogen gas. Materials Research, 25, e20210575. https://doi.org/10.1590/1980-5373-mr-2021-0575
10. Moon, J., & Sahajwalla, V. (2006). Investigation into the role of the boudouard reaction in self-reducing iron oxide and carbon briquettes. Metallurgical and Materials Transactions B, 37(2), 215-221. https://doi.org/10.1007/bf02693151
11. Nikolov, T. G., & Kolchanov, V. (1980). The Decarburization of Cast Iron Products in a Gas Phase. Izv. V. U. Z. Chernaya Metall., (3), 19-23.
12. Setiawan, A., Harjanto, S., Kawigraha, A., Ikhwani, N., & Rhamdhani, M. A. (2023). Microstructure Evolution and Phase Transformation of Iron Produced from the Sustainable Carbothermic Reduction Process of High-Pressure Acid Leaching Residue. ACS omega, 8(42), 39651-39661. https://doi.org/10.1021/acsomega.3c05574
13. Chen, C., Wang, T., Wei, S., Mao, F., Liu, W., Xiong, M., & Zhang, C. (2022). The Influence of Ni Content on the Microstructure and Impact Wear Resistance Performance of High-Chromium Casting Infiltration Coating. Coatings, 12(9), 1313. https://doi.org/10.3390/coatings12091313

Review Article

The Invisible Enemy: Nanoparticle Exposure and Neurodegenerative Decline

Aytaj S. Hasanova[1] **and Fatima S. Hasanova**[2]

[1]Department of Mechanics and Mathematics, School of Advanced Technologies and Innovation Engineering, Western Caspian University, 17A Ahmad Rajabli Street, III Parallel, AZ1001 Baku, Azerbaijan
[2]Department of Emergency and Mobile Medical Care, Central Clinic Hospital (Research Collaboration), 76 Parliament Avenue, AZ1006 Baku, Azerbaijan

Received: 06.11.2025 Accepted: 14.11.2025 Published: 19.11.2025

https://doi.org/10.54414/FKVT6156

Abstract

Atmospheric air pollution, specifically the ultra-fine fraction of particulate matter ($PM_{2.5}$) known as nanoparticles (NPs), poses serious global health threats with critical neurological implications. This review summarizes evidence indicating that inhaled nanoparticles, particularly metallic nanoparticles (MNPs), can penetrate respiratory defense mechanisms and the blood-brain barrier (BBB). This enables direct translocation into the central nervous system (CNS). Once they enter the brain, these nanoparticles act as structural scaffolds, thereby accelerating the misfolding and aggregation of amyloid-beta (Aβ) peptides. This phenomenon has been identified as a pathological hallmark of Alzheimer's disease (AD). The underlying mechanisms involve chronic neuroinflammation and excessive reactive oxygen species (ROS) generation, leading to neuronal degeneration and cognitive decline. Significantly, the physicochemical properties that make nanoparticles potentially hazardous also present therapeutic possibilities. A notable example is the use of gold nanoparticles (AuNPs) to inhibit amyloid beta aggregation, which highlights the potential of nanomedicine for targeted neuroprotection.

Keywords: air pollution, particulate matter ($PM_{2.5}$), nanoparticles (NPs), amyloid beta (Aβ) protein, neurotoxicity, Alzheimer's disease (AD), reactive oxygen species (ROS)

1. Introduction

The population growth and development of industry have created various types of pollution. Among these pollutions, air pollution has become one of the main global problems around the world. The consequences of polluted air led to adverse health effects in humans and other living organisms. In addition to that, the polluted air is damaging the ecosystem and contributing to climate change. The substances that cause this air pollution are toxic chemicals such as sulfur dioxide (SO_2) or nitrogen oxides (NO and NO_2) emitted from vehicles, and particulate matter (PM) in the atmosphere [1].

Air pollution comes from both natural sources, such as volcanic eruptions, wildfires, and desert dust, and human-made sources such as biomass burning, industry smog, vehicle exhaust, power generation, and construction activity, which are a great percentage of air pollution. According to this, human activity is often associated with polluted air in many urban areas. The main difference between the two of them is that natural sources cannot be controlled, in contrast to human activities. Depending on the harmful substances, air pollution can occur inside the building, called indoor air pollution, and outside the building, called outdoor air pollution. The majority of indoor air pollution is caused by human activities. Nevertheless, both natural sources and human-made sources are outdoor pollutants [2]. The statistics published by the World Health Organization (WHO) show that 9 out of 10

people in the world are exposed to polluted air. It results in around 7 million deaths each year because of complications arising from indoor and outdoor air pollution [3].

The historical record contains numerous documented incidents of air pollution, including the Donora Smog in the United States in 1948, which led to respiratory disorders and 20 fatalities [4], and the Great Smog of London in the United Kingdom in 1952. The combination of industrial pollution and domestic coal burning (Figure 1) led to an estimated 12,000 deaths, prompting the UK government to introduce the first "Clean Air Act" (CAA) in 1956 [5]. The main goal of the act was to set new standards, take measures to decrease air pollution, and protect the environment. Therefore, the CAA implemented a decision to make the use of smokeless fuels mandatory.

Figure 1. Great Smog of London [5].

In the present age, advanced monitoring programs such as the National Air Quality Monitoring Program (NAMP) and the Air Quality Index (AQI), frequently enhanced by artificial intelligence (AI) and machine learning (ML), are employed to track and manage air quality in real time [6].

2. Particulate Matter (PM) Fractions and Their Biological Penetration

Particulate matter is a mixture of microscopic particles in the air that are composed of solids and liquids and can harm human health. It is responsible for human morbidity and mortality. Particle pollution of air can be found both indoors (induced during home activities, renovation works, and indoor workshop activities) and outdoors (traffic, industry) (Figure 2) [7]. PM accumulation affects soil and water quality, which can affect plant and animal life. It is classified based on particle size, PM_{10} (coarse particles, ≤10 μm) and $PM_{2.5}$ (fine particles, ≤2.5 μm) [8].

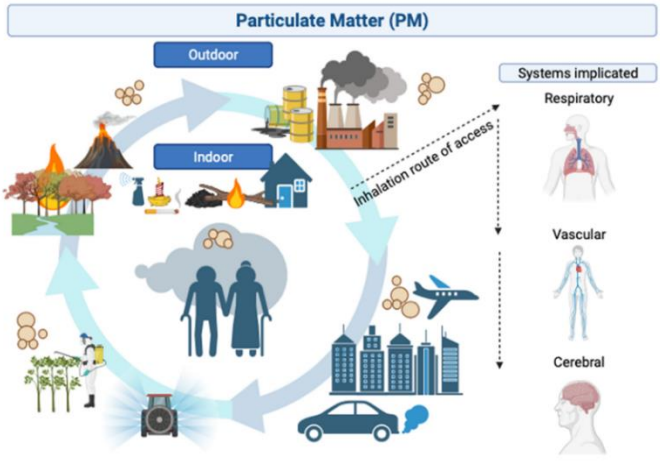

Figure 2. Graphical representation of PM in indoor and outdoor environments [7].

2.1. Biological Penetration of PM_{10}

PM_{10} is particulate matter that is 10 µm or less in diameter. However, it may still be visible to the naked eye under some circumstances as dust. Compared to $PM_{2.5}$, PM_{10} is heavier and falls to the ground more quickly, and it can cause discomfort in the eyes and nose. Over and above, it does not penetrate the lungs as deeply as $PM_{2.5}$. Respiratory and cardiovascular diseases are associated with PM_{10} exposure. The main causes of PM_{10} are transportation and industrial activities. Forests and green areas are significant as cleaning factors to prevent PM_{10} [9].

2.2. Biological Penetration of $PM_{2.5}$

$PM_{2.5}$ is particulate matter that is 2.5 µm or below in size and consists of ultra-fine particles and nanoparticles. They are not visible and come from a variety of sources, such as vehicle emissions, manufacturing facilities, power generation, and construction activities.

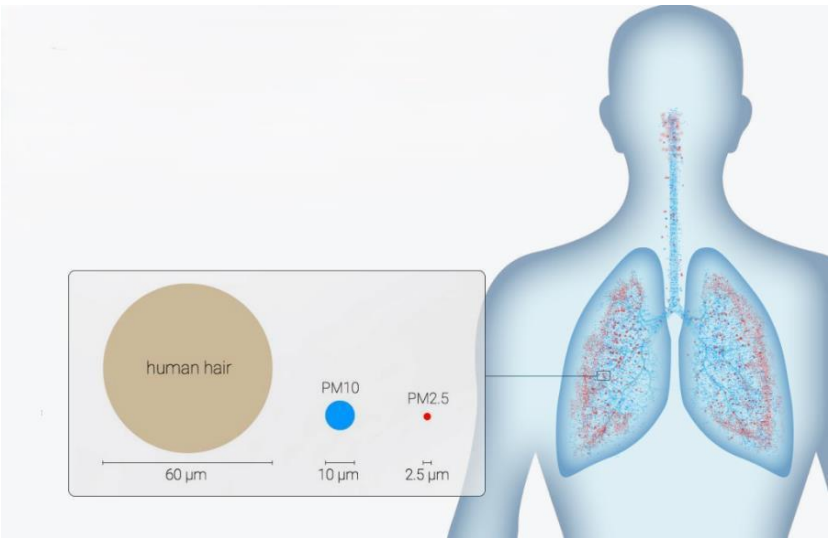

Figure 3. Graphical representation of PM_{10} and $PM_{2.5}$ [10].

Due to their microscopic size, they can be hard to prevent, may easily penetrate the body, affect its circulation and the breathing systems, and result in damage to the lungs (Figure 3) [10], heart, and brain. Table 1 illustrates disorders associated with $PM_{2.5}$ exposure [11].

Table 1. List of diseases caused by $PM_{2.5}$.

Health Effect	Associated Disorders
Respiratory diseases	Sore throat, asthma, bronchitis, tuberculosis, Chronic Obstructive Pulmonary Disease (COPD), pneumonia, lung cancer, head and neck cancer [12]
Cardiovascular diseases	Heart attacks, strokes, arrhythmias, ischemic heart disease, hypertension, atherosclerosis [13]
Neurodegenerative diseases	Dementia, Alzheimer's disease, Parkinson's disease [14]
Other health effects	Tiredness, headache, reduced intellectual ability, and premature death [15]

3. Global Monitoring of $PM_{2.5}$

The global challenge of controlling $PM_{2.5}$ underscores the necessity for international collaboration, where countries and international organizations must prioritize the mitigation of industrial emissions, the promotion of clean energy sources, and the promotion of sustainable transportation.

3.1. Regional Pollution in Asia

The presence of $PM_{2.5}$ pollution in Asia indicates a significant environmental crisis. According to the AQI 2022 ranking [16] and the 2019 World Air Quality Report [10], a considerable number of the world's most air-polluted countries are located in Asia (Figure 4).

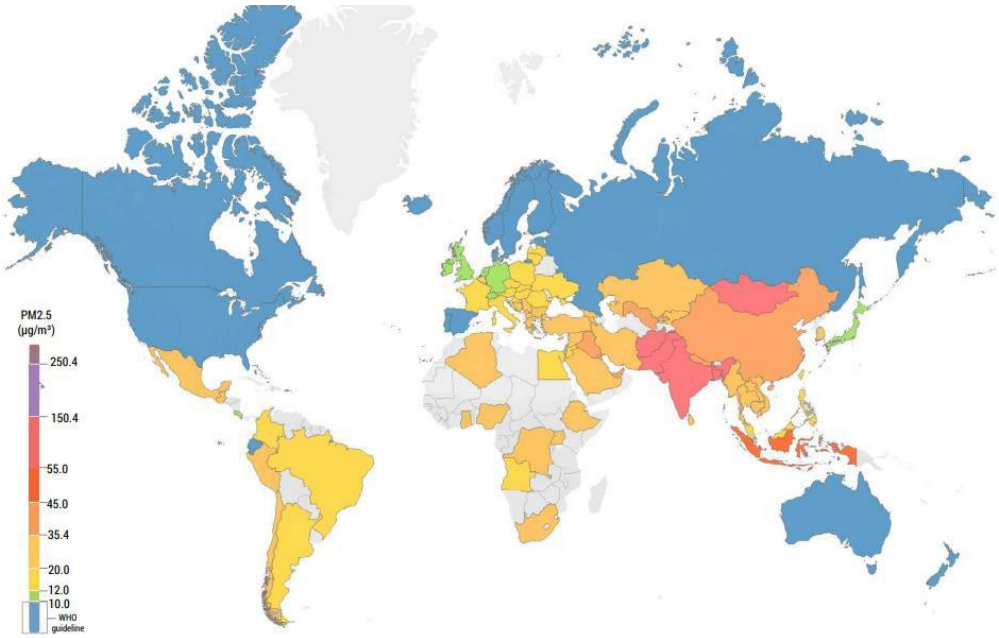

Figure 4. Global map of countries exposed by $PM_{2.5}$ in 2019 [10].

Table 2 presents the countries and their cities affected by $PM_{2.5}$ and the reasons that played the biggest role in its creation.

Table 2. List of Asian countries, the most polluted cities, and the biggest sources.

Countries	The most polluted cities	The biggest sources
Bangladesh	Dhaka	Brickmaking industry, motor vehicles, wood burning, soil, and road dust [17]
Pakistan	Punjab	Transportation, industry emissions, and power generation [18]
India	Delhi	Industryand manufacturing, vehicle emissions [19]
China	Beijing	Industrial and energy structure, vehicle exhaust, and coal combustion [20]
Thailand	Chiang Rai	Manufacturing, power plants, vehicles, and agricultural burning [21]

According to the 2018 publication by WHO, there were 543000 fatalities in children under the age of 5 and 52000 deaths in children aged 5 to 15 because of polluted air in 2016. The fact that the number of deaths in children is higher than in adults [22]. The main reason is that the absorption of contaminants is due to engaging in air activities for a long time.

3.2. Regional Pollution in Europe

Contrary to the higher air quality standards generally maintained by European countries, significant regional challenges remain, particularly in Eastern Europe. In 2015, researchers documented 449,813 premature deaths in Europe [23] that were associated with $PM_{2.5}$ from anthropogenic sources, with agricultural emissions, vehicles, and home heating recognized as primary contributors.

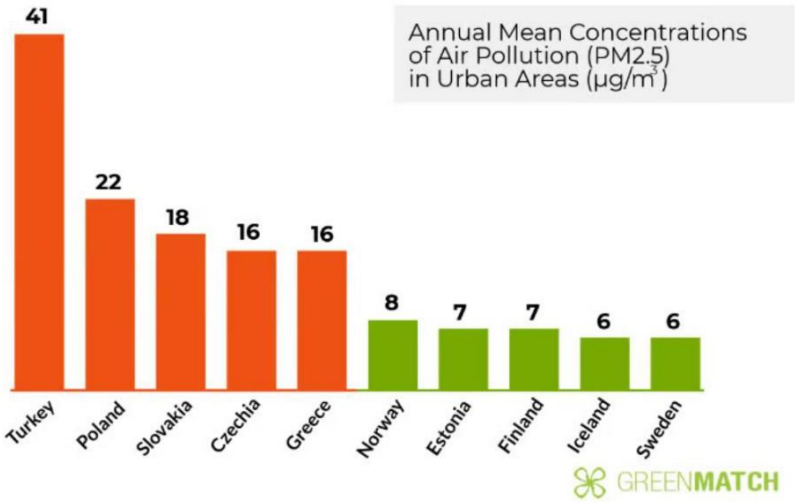

Figure 5. European countries' $PM_{2.5}$ concentrations by GreenMatch [24].

According to the "Green Match", European countries such as Poland, Slovakia, Czechia, Turkey (3% European portion), and Greece are significantly affected by air pollution $PM_{2.5}$. Figure 5 represents the annual mean concentrations of the $PM_{2.5}$ fraction in air pollution in urban areas of European countries. Turkey leads the list, followed by Poland. The main reasons are industry, transport, carbon dioxide production from other sources, and a lack of green areas. Air pollution is very low and controlled in countries like Norway, Sweden, and Finland compared to Turkey [24].

4. Nanoparticles as a Key Component of $PM_{2.5}$

The concept of "Particulate Matter" (PM), particularly the subcategory $PM_{2.5}$, serves as a comprehensive classification system for heterogeneous atmospheric pollutants. Nevertheless, the most biologically reactive and hazardous component of this mixture is the ultrafine fraction, also known as nanoparticles (NPs). According to the accepted definition, nanoparticles range from 1 to 100 nanometers (nm) and represent a high-hazard component that is unequally disproportionate to their mass concentration. These substances are derived from both naturally occurring sources and anthropogenic emissions, particularly those resulting from high-temperature combustion processes (vehicular exhaust and industrial activities) that generate metallic, metal oxide, and organic compounds [25].

The primary risk posed by nanoparticles derives from their particular physicochemical characteristics. Their large surface area relative to volume enhances chemical reactivity, promoting the generation of reactive oxygen species (ROS) and other damaging cellular molecules. Due to their ultrafine size, nanoparticles have the capacity to penetrate deeply into the respiratory tract and efficiently cross the alveolar–capillary barrier [26], a phenomenon that larger particulate matter fractions are generally unable to do. Once translocated into the blood-brain barrier (BBB), they can diffuse systemically, carrying toxic metals, organic compounds, and other adsorbent

pollutants to distant organs. This systemic process converts localized air pollution exposure into a threat that affects the entire body, with particular exposure to the central nervous system (CNS). In this system, nanomaterials have been observed to induce neuroinflammation and oxidative stress [27].

5. The Potential Influence of Nanoparticles on Amyloid Beta Protein

The impact of nanoparticles (NPs) on proteins is also necessary, depending on the shape, size, and surface charge of nanoparticles. Small nanoparticles have a large surface area-to-volume ratio. It means that they can penetrate biological barriers and interact with proteins more easily. Additionally, small nanoparticles are so active based on their high surface area, and they can cause oxidative stress and inflammation, leading to greater neuronal damage and increased neurotoxicity. Large nanoparticles have a lower surface area-to-volume ratio. It means that they cannot penetrate biological barriers so easily. They can have limited protein-surface interactions. It means less oxidative stress and reduced neurotoxicity [28].

Nanoparticles in $PM_{2.5}$ have a profound effect on many proteins, including amyloid beta (Aβ) and human cystatin C. These particles can also cause oxidative stress by producing reactive oxygen species (ROS). The formation of reactive oxygen species causes cellular, protein, and DNA damage, which creates mutations. In the end, these proteins change their structure and denature or lose their functionality. Many diseases, such as cancer, cardiovascular, respiratory, and neurodegenerative disorders, occur as a consequence of the deterioration of these proteins. Studies in mice have concluded that zinc, iron, and copper are directly related to the development of amyloid plaques in neurodegenerative disorders and cause increased oxidative stress and neuronal dysfunction [29]. Moreover, other studies have provided strong evidence that copper, zinc, and iron contribute to the development of Alzheimer's disease in terms of the aggregation of amyloid beta proteins and the generation of reactive oxygen species (Figure 6) [30, 31].

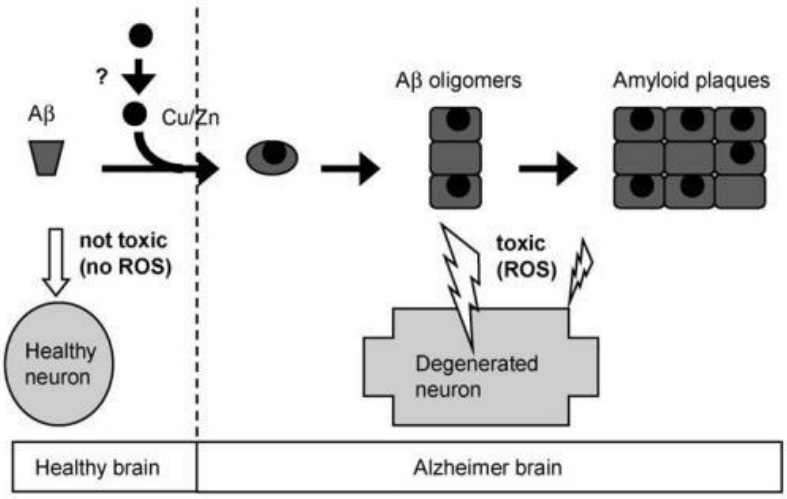

Figure 6. An illustration of neural defects [31].

6. Amyloid Beta Protein as a Key Component of Alzheimer's Disease

Amyloid beta (Aβ) peptide is derived from the amyloid precursor protein (APP), which is a large protein in the central nervous system (CNS) and is linked to Alzheimer's disease (AD). Amyloid beta exists in a random coil shape or α-helical and typically consists of approximately 35-43 amino acids [32]. As a result of the environmental impact (air pollution), genetic mutations (age, neuronal death), and lifestyle factors (lack of exercise and poor diet), protein abnormalities appear. In this case, amyloid beta can misfold into an aberrant shape spontaneously. The aggregation of these abnormal proteins leads to the formation of small oligomers, which harmfully influence the cells and speed up the development of disorders. Finally, the aggregation of these oligomers creates long fibrils (Figure 7) [33] that are distinguished by their cross-beta sheet structure and are

extremely stable. Briefly, the amyloid beta peptide is the key point of oligomerization and fibrillogenesis that contributes to the development of Alzheimer's disease [34].

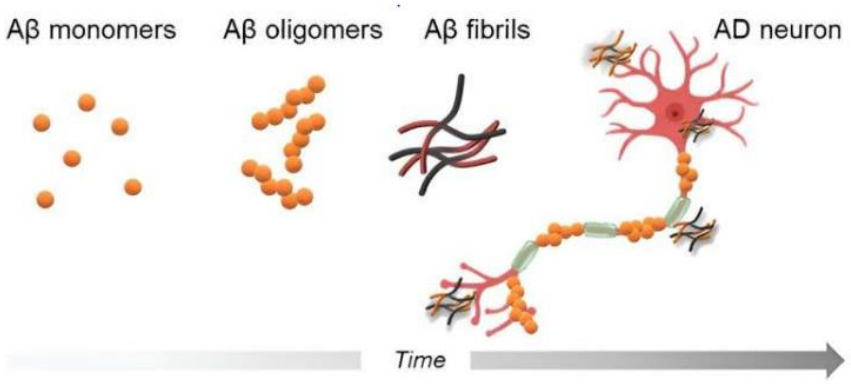

Figure 7. Alzheimer's Disease Mechanism [33].

Alzheimer's disease is a neurodegenerative disorder associated with the amyloidogenesis process. This process (according to the amyloid hypothesis) is linked to the degradation and death of brain cells, leading to Alzheimer's disease. Firstly, it begins with dementia, which means poor memory and declined cognition. Based on research in London, it is suggested that living near the main roads in the city center increases the risk of dementia [35]. Air pollution caused by traffic, which contains particulate matter ($PM_{2.5}$), has a strong effect on cognitive decline [36], particularly in children.

Plaques and tangles are the abnormal protein deposits in the brain that provoke Alzheimer's disease. These deposits are composed of two main proteins known as amyloid beta, which is found around the neurons, and tau, which is found inside the neurons. Normally, amyloid beta and tau are present in healthy brains; however, their functions are deviant in Alzheimer's disease. Neurofibrillary tangles are composed of tau protein, and amyloid plaques are composed of amyloid beta protein, which is part of the amyloid precursor protein. Tangles and plaques destroy many nerve cells, causing cell death and, consequently, the brain begins to shrink. The key symptoms of Alzheimer's disease are memory loss, cognitive disabilities, and behavior problems [37].

7. Dual Roles of Nanoparticles

Despite their hazardous association with particulate matter (PM) and protein aggregation, some nanoparticles are being studied for therapeutic applications. Their distinctive characteristics, including precise size control and surface chemistry, qualify them as optimal candidates for drug targeting and delivery. For instance, studies have examined the potential of certain gold nanoparticles to regulate the aggregation of amyloid beta peptides, providing a promising perspective for future Alzheimer's disease therapeutic approaches. Similarly, carbon-based nanomaterials, including graphene quantum dots and polymeric nanoparticles, have exhibited inhibitory effects on amyloid beta (Aβ) fibrillation and enhanced blood-brain barrier transport in earlier research studies. [38, 39].

8. Conclusion and Future Directions

The findings of this study provide substantial evidence that ultrafine particulate matter and the metallic nanoparticles it harbors are not merely respiratory irritants but rather systemic toxicants capable of inducing significant neurological and cellular damage. The precise mechanism by which these nanoparticles stimulate the misfolding and aggregation of amyloid beta is a critical area of research. It is crucial to comprehend the dual nature of nanoparticles, which serve both as environmental contaminants and as prospective therapeutic agents. This understanding is fundamental to the development of effective public health policies aimed at reducing exposure, as well as the creation of innovative nanomedicines for the treatment of neurodegenerative disorders.

Author Contributions

The authors confirm responsibility for the conception, drafting, critical revision, and final approval of the manuscript.

Conflict of Interest

The authors declare no conflicts of interest.

Funding

This research was not supported by external funding.

Acknowledgment

The authors would like to thank Adam Mickiewicz University for technical support and Prof. Dr. Maciej Kozak for insightful discussions.

Data Availability Statement

The authors declare that the data supporting the findings of this study are available within the article.

Abbreviations

Sulfur Dioxide (SO_2), Nitrogen Oxides (NO and NO_2), World Health Organization (WHO), Clean Air Act (CAA), National Air Quality Monitoring Program (NAMP), Air Quality Index (AQI), Artificial Intelligence (AI), Machine Learning (ML), Particulate Matter (PM), Nanometers (nm), Chronic Obstructive Pulmonary Disease (COPD), Nanoparticles (NPs), Metallic Nanoparticles (MNPs), Central Nervous System (CNS), Reactive Oxygen Species (ROS), Blood-Brain Barrier (BBB), Amyloid Beta (Aβ), Amyloid Precursor Protein (APP), Alzheimer's Disease (AD).

References

1. Shetty, S. S., Deepthi, D., Harshitha, S., Sonkusare, S., Naik, P. B., & Madhyastha, H. (2023). Environmental pollutants and their effects on human health. *Heliyon*,*9*(9). https://doi.org/10.1016/j.heliyon.2023.e19496
2. Leung, D. Y. (2015). Outdoor-indoor air pollution in urban environment: challenges and opportunity. *Frontiers in Environmental Science*,*2*, 69. https://doi.org/10.3389/fenvs.2014.00069
3. Bilal, M., Mhawish, A., Nichol, J. E., Qiu, Z., Nazeer, M., Ali, M. A., & Ke, S. (2021). Air pollution scenario over Pakistan: Characterization and ranking of extremely polluted cities using long-term concentrations of aerosols and trace gases. *Remote Sensing of Environment*, *264*, 112617. https://doi.org/10.1016/j.rse.2021.112617
4. Jacobs, E. T., Burgess, J. L., & Abbott, M. B. (2018). The Donora smog revisited: 70 years after the event that inspired the clean air act. *American journal of public health*, *108*(S2), S85-S88. https://doi.org/10.2105/ajph.2017.304219
5. Polivka, B. J. (2018). The great London smog of 1952. *AJN The American Journal of Nursing*, *118*(4), 57-61. https://doi.org/10.1097/01.naj.0000532078.72372.c3
6. Singh, D., Dahiya, M., Kumar, R., & Nanda, C. (2021). Sensors and systems for air quality assessment monitoring and management: A review. *Journal of environmental management*, *289*, 112510. https://doi.org/10.1016/j.jenvman.2021.112510
7. López-Granero, C., Polyanskaya, L., Ruiz-Sobremazas, D., Barrasa, A., Aschner, M., & Alique, M. (2023). Particulate matter in human elderly: higher susceptibility to cognitive decline and age-related diseases. *Biomolecules*, *14* (1), 35. https://doi.org/10.3390/biom14010035

8. U.S. Environmental Protection Agency. (2025, March 8). Particulate matter (PM) basics. https://www.epa.gov/pm-pollution/particulate-matter-pm-basics
9. Sohrab, S., Csikos, N., & Szilassi, P. (2023). Effects of land use patterns on PM10 concentrations in urban and suburban areas. A European scale analysis. *Atmospheric Pollution Research*, *14*(12), 101942. https://doi.org/10.1016/j.apr.2023.101942
10. IQAir. (2019). *2019 World Air Quality Report.* https://www.iqair.com/dl/pdf-reports/2019-World-Air-Report-V8-20200318.pdf
11. Thangavel, P., Park, D., & Lee, Y. C. (2022). Recent insights into particulate matter (PM2. 5)-mediated toxicity in humans: an overview. *International journal of environmental research and public health*, *19*(12), 7511. https://doi.org/10.3390/ijerph19127511
12. Simkovich, S. M., Goodman, D., Roa, C., Crocker, M. E., Gianella, G. E., Kirenga, B. J., & Checkley, W. (2019). The health and social implications of household air pollution and respiratory diseases. *NPJ primary care respiratory medicine*, *29*(1), 12. https://doi.org/10.1038/s41533-019-0126-x
13. Al-Kindi, S. G., Brook, R. D., Biswal, S., & Rajagopalan, S. (2020). Environmental determinants of cardiovascular disease: lessons learned from air pollution. *Nature Reviews Cardiology*, *17*(10), 656-672. https://doi.org/10.1038/s41569-020-0371-2
14. Shou, Y., Huang, Y., Zhu, X., Liu, C., Hu, Y., & Wang, H. (2019). A review of the possible associations between ambient PM2. 5 exposures and the development of Alzheimer's disease. *Ecotoxicology and Environmental Safety*, *174*, 344-352. https://doi.org/10.1016/j.ecoenv.2019.02.086
15. Shi, Y., Zhao, A., Matsunaga, T., Yamaguchi, Y., Zang, S., Li, Z., & Gu, X. (2018). Underlying causes of PM2. 5-induced premature mortality and potential health benefits of air pollution control in South and Southeast Asia from 1999 to 2014. *Environment international*, *121*, 814-823. https://doi.org/10.1016/j.envint.2018.10.019
16. IQAir. (2023). *World's most polluted countries & regions.* https://www.iqair.com/us/world-most-polluted-countries
17. Begum, B. A., & Hopke, P. K. (2019). Identification of sources from chemical characterization of fine particulate matter and assessment of ambient air quality in Dhaka, Bangladesh. *Aerosol and air quality research*, *19*(1), 118-128. https://doi.org/10.4209/aaqr.2017.12.0604
18. Anjum, M. S., Ali, S. M., Subhani, M. A., Anwar, M. N., Nizami, A. S., Ashraf, U., & Khokhar, M. F. (2021). An emerged challenge of air pollution and ever-increasing particulate matter in Pakistan; a critical review. *Journal of Hazardous Materials*, *402*, 123943. https://doi.org/10.1016/j.jhazmat.2020.123943
19. Selokar, A., Ramachandran, B., Elangovan, K. N., & Varma, B. D. (2020). PM 2.5 particulate matter and its effects in Delhi/NCR. *Materials Today: Proceedings*, *33*, 4566-4572. https://doi.org/10.1016/j.matpr.2020.08.187
20. Pang, N., Gao, J., Zhu, G., Hui, L., Zhao, P., Xu, Z., & Chai, F. (2021). Impact of clean air action on the PM2. 5 pollution in Beijing, China: Insights gained from two heating seasons measurements. *Chemosphere*, *263*, 127991. https://doi.org/10.1016/j.chemosphere.2020.127991
21. Supasri, T., Gheewala, S. H., Macatangay, R., Chakpor, A., & Sedpho, S. (2023). Association between ambient air particulate matter and human health impacts in northern Thailand. *Scientific Reports*, *13*(1), 12753. https://doi.org/10.1038/s41598-023-39930-9
22. Anwar, A., Ullah, I., Younis, M., & Flahault, A. (2021). Impact of air pollution (PM2. 5) on child mortality: Evidence from sixteen Asian countries. *International journal of environmental research and public health*, *18*(12), 6375. https://doi.org/10.3390/ijerph18126375
23. Gu, Y., Henze, D. K., Nawaz, M. O., Cao, H., & Wagner, U. J. (2023). Sources of PM2. 5-associated health risks in Europe and corresponding emission-induced changes during 2005–2015. *GeoHealth*, *7*(3), e2022GH000767. https://doi.org/10.1029/2022gh000767
24. GreenMatch. (2018). *Mapped: Europe's most and least polluted countries.* GreenMatch UK. https://www.greenmatch.co.uk/blog/2018/11/mapped-europes-most-and-least-polluted-countries
25. Horikoshi, S. A. T. O. S. H. I., & Serpone, N. I. C. K. (2013). Introduction to nanoparticles. *Microwaves in nanoparticle synthesis: fundamentals and applications*, 1-24. https://doi.org/10.1002/9783527648122.ch1

26. Oberdörster, G., Oberdörster, E., & Oberdörster, J. (2005). Nanotoxicology: an emerging discipline evolving from studies of ultrafine particles. *Environmental health perspectives*, *113*(7), 823-839. https://doi.org/10.1289/ehp.7339
27. Genc, S., Zadeoglulari, Z., Fuss, S. H., & Genc, K. (2012). The adverse effects of air pollution on the nervous system. *Journal of toxicology*, *2012*(1), 782462. https://doi.org/10.1155/2012/782462
28. Buzea, C., & Pacheco, I. (2019). Toxicity of nanoparticles. In *Nanotechnology in eco-efficient construction* (pp. 705-754). Woodhead Publishing. https://doi.org/10.1016/b978-0-08-102641-0.00028-1
29. James, S. A., Churches, Q. I., de Jonge, M. D., Birchall, I. E., Streltsov, V., McColl, G., & Hare, D. J. (2017). Iron, copper, and zinc concentration in Aβ plaques in the APP/PS1 mouse model of Alzheimer's disease correlates with metal levels in the surrounding neuropil. *ACS chemical neuroscience*, *8*(3), 629-637. https://doi.org/10.1021/acschemneuro.6b00362
30. Faller, P. (2009). Copper and zinc binding to amyloid-β: coordination, dynamics, aggregation, reactivity and metal-ion transfer. *ChemBioChem*, *10*(18), 2837-2845. https://doi.org/10.1002/cbic.200900321
31. Tougu, V., Karafin, A., & Palumaa, P. (2008). Binding of zinc (II) and copper (II) to the full-length Alzheimer's amyloid-β peptide. *Journal of neurochemistry*, *104*(5), 1249-1259. https://doi.org/10.1111/j.1471-4159.2007.05061.x
32. Hane, F., Tran, G., Attwood, S. J., & Leonenko, Z. (2013). Cu2+ affects amyloid-β (1–42) aggregation by increasing peptide-peptide binding forces. *PloS one*, *8*(3), e59005. https://doi.org/10.1371/journal.pone.0059005
33. Medical Xpress. (2024, March). *Nanoparticles activated by ultra-low-energy X-rays halt aggregation, toxicity of amyloid beta in preclinical models*. https://medicalxpress.com/news/2024-03-nanoparticles-ultra-energy-rays-halt.html#google_vignette
34. Jan, A., Hartley, D. M., & Lashuel, H. A. (2010). Preparation and characterization of toxic Aβ aggregates for structural and functional studies in Alzheimer's disease research. *Nature protocols*, *5*(6), 1186-1209. https://doi.org/10.1038/nprot.2010.72
35. Carey, I. M., Anderson, H. R., Atkinson, R. W., Beevers, S. D., Cook, D. G., Strachan, D. P., & Kelly, F. J. (2018). Are noise and air pollution related to the incidence of dementia? A cohort study in London, England. *BMJ open*, *8*(9), e022404. https://doi.org/10.1136/bmjopen-2018-022404
36. Tang, Y., Li, Z., Fu, Y., & Zhao, M. (2024). Causal Effects of PM2. 5, NOx, and NO2 on Cognitive Function: A Two-sample Mendelian Randomization Study. *Aerosol and Air Quality Research*, *24*(8), 230326. https://doi.org/10.4209/aaqr.230326
37. Scheltens, P., De Strooper, B., Kivipelto, M., Holstege, H., Chételat, G., Teunissen, C. E., & van der Flier, W. M. (2021). Alzheimer's disease. *The Lancet*, *397*(10284), 1577-1590. https://doi.org/10.1016/s0140-6736(20)32205-4
38. Huang, Y., Chang, Y., Liu, L., & Wang, J. (2021). Nanomaterials for modulating the aggregation of β-amyloid peptides. *Molecules*, *26*(14), 4301. https://doi.org/10.3390/molecules26144301
39. Abbas, M. (2021). Potential role of nanoparticles in treating the accumulation of amyloid-beta peptide in Alzheimer's patients. *Polymers*, *13*(7), 1051. https://doi.org/10.3390/polym13071051

Review Article

Investigation of Elastomeric Seal Systems in Oil and Gas Well Applications

Gulnar A. Hamidova[1] and Saida A. Abdurahimova[2]

[1, 2]Department of Mechanics and Mathematics, School of Advanced Technologies and Innovation Engineering, Western Caspian University, 17A Ahmad Rajabli Street, III Parallel, AZ1001 Baku, Azerbaijan

Received: 05.11.2025 Accepted: 18.11.2025 Published: 19.11.2025

https://doi.org/10.54414/VVRP7015

Abstract

The article provides a detailed review of literature, research findings, and industrial standards related to elastomer seal assemblies used in oil and gas wells. Elastomer-based seals are essential for maintaining well integrity. Advances in rubber chemistry and sealing technologies were critical in controlling pressure and fluid flow long before the 1901 Spindletop oil eruption in Texas. These materials remain indispensable today, as the cost of constructing a single well can exceed one billion dollars. Almost all modern drilling and completion systems rely on elastomers and other sealing materials to ensure reliable operation throughout their service life. Research shows that seal malfunctions can cause blowouts or oil leaks, creating serious health, safety, and environmental risks. Because of these risks, regulators and industry experts stress the need for improved seal design and qualification, especially for high-pressure, high-temperature (HPHT) applications. This paper evaluates key studies and standards on elastomer sealing systems. It examines the main factors that influence seal performance and the major causes of failure. The review's primary aim is to identify gaps in current standards and propose priority areas for future research to improve seal reliability. The analytical results show how elastomer geometry and material properties influence maximum sealing pressure. The study also analyzes different strain conditions to assess sealing efficiency. Current industry standards focus mainly on material-level testing and offer limited guidance for seal design within complete equipment assemblies. Existing qualification procedures are not well adapted to different seal shapes, sizes, or applications. More comprehensive research is needed on seal assembly design, including energization mechanisms, housing and support structures, and potential functional failures—going beyond basic material evaluation. Furthermore, there is a pressing need for robust methodologies capable of translating laboratory-scale findings into field-level applications that ensure long-term operational reliability.

Keywords: elastomer seal, seal assessment, industry standards, well barriers, well integrity, seal failure

1. Introduction

To ensure effective well control, seal assemblies located in wellheads or liners act as critical barrier elements [1, 2]. These seals typically serve as secondary barriers that prevent formation fluids from entering the wellbore. The primary barrier is the annular cement sheath. Together, the cement sheath and the seal assembly form a dual-barrier system. However, during well construction, it is not possible to pressure-test these two barriers independently. Instead, they must be evaluated as a single integrated system. As a result, a successful pressure test only confirms that at least one barrier is functioning, without identifying which one.

The cement sheath is generally considered less reliable as a standalone barrier because of factors such as inherent permeability, potential gas migration, poor bonding, and the formation of microannuli [3]. In some cases, the seal assembly may compensate for deficiencies in the cement sheath during pressure testing. In such situations,

the seal assembly effectively becomes the only dependable pressure-holding element. This outcome highlights the need for seal assemblies with high long-term reliability to ensure overall well integrity.

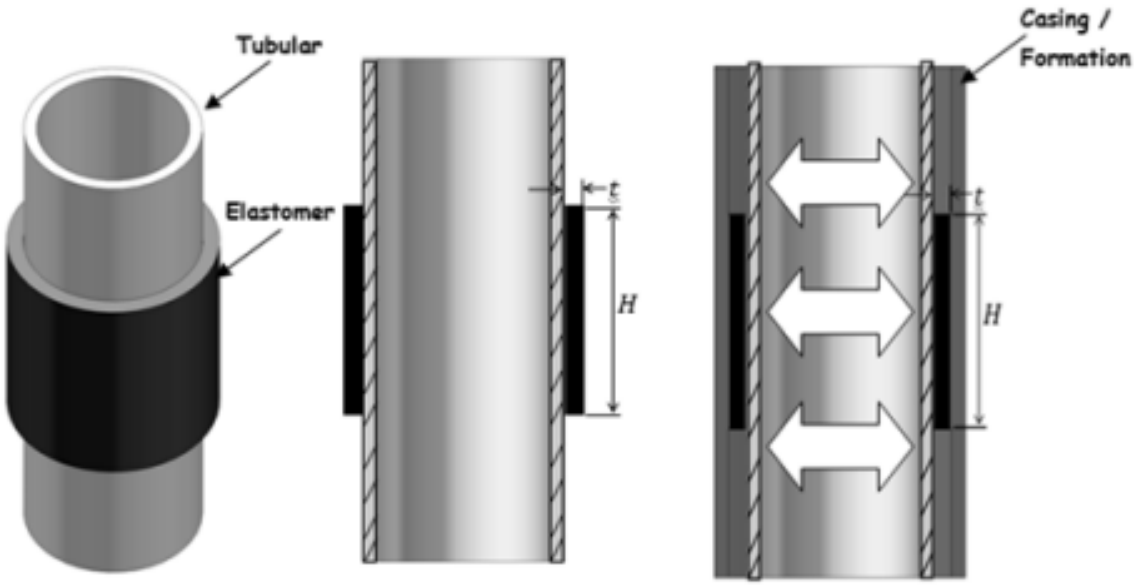

Figure 1. Schematic of a typical swellable packer.

It has been observed that failures in seal assemblies are often a key factor behind well-control incidents that can result in serious consequences for human health, safety, and the environment. An informal evaluation conducted among several operators in the Gulf of Mexico revealed that the failure rate of pressure seals in liner overlaps ranges between 30% and 50%. Another study highlighted growing concerns regarding the reliability of critical liner-hanger seals, particularly in high-pressure, high-temperature (HPHT) completions. Globally, it is estimated that approximately 18% of offshore wells exhibit some degree of uncertainty or weakness related to their seal assemblies [4].

The Bureau of Safety and Environmental Enforcement (BSEE), the primary regulatory authority, has also raised concerns about the reliability of elastomer-based seal assemblies. Through a technical evaluation, the agency emphasized the need for additional research focusing on the design, performance reliability, and service-life assessment of these sealing systems, especially those used in liner-hanger applications.

2. Objective

Elastomer seals are increasingly utilized across multiple sectors, including the oil and gas industry. This review aims to achieve four main objectives [5]: (1) to identify and analyze potential failure mechanisms in elastomer seal assemblies; (2) to review relevant experimental, theoretical, and computational studies; (3) to examine various parameters influencing the performance of sealing systems; and (4) to conduct a gap analysis of current industry standards and practices. Furthermore, the study seeks to pinpoint critical knowledge gaps to guide future research aimed at improving the design and dependability of elastomer seals.

This review serves as a valuable reference for regulators, researchers, engineers, and industry professionals. By understanding possible failure mechanisms, engineers and product developers can design more robust and reliable seal assemblies. A comprehensive analysis of existing literature and identified research gaps will help steer future investigations. Additionally, performing a gap analysis of current standards enables both industry and regulatory bodies to strengthen guidelines, certification procedures, and policies concerning the qualification and use of elastomer seal assemblies.

3. Seal Assemblies

The likelihood of equipment containing elastomer seals being present during different well operations can be evaluated. Studies have shown that, compared to packers and subsurface safety valves (SSSVs), wellhead and blowout preventer (BOP) systems are significantly more likely to be involved when a blowout occurs. In fact, wellhead components such as casing or liner hangers are always part of the well infrastructure, regardless of the well type.

In many cases, operators prefer to deploy a liner string rather than running a full casing string back to the wellhead [6]. The liner is typically suspended from the preceding casing and cemented in place. Similar to casing hangers, liner hangers also contain seal assemblies. These hanger seals are generally installed on the exterior of each casing or liner string to isolate the annular spaces.

A conventional liner hanger assembly typically consists of three main components: a cone or compression plate, an elastomer sealing element, and slips (as shown in Fig. 2a and Fig. 2b). Depending on the design, the seal assembly may either be incorporated into the liner running tool (Fig. 2b) or installed separately, which requires an additional trip into the well (Fig. 2a). The seal assembly is activated by applying either hydraulic or mechanical axial force that sets the slips against the corresponding surface. When axial load is further increased while the lower compression plate is held in position by the slips, the elastomer element becomes compressed, thereby creating the necessary seal.

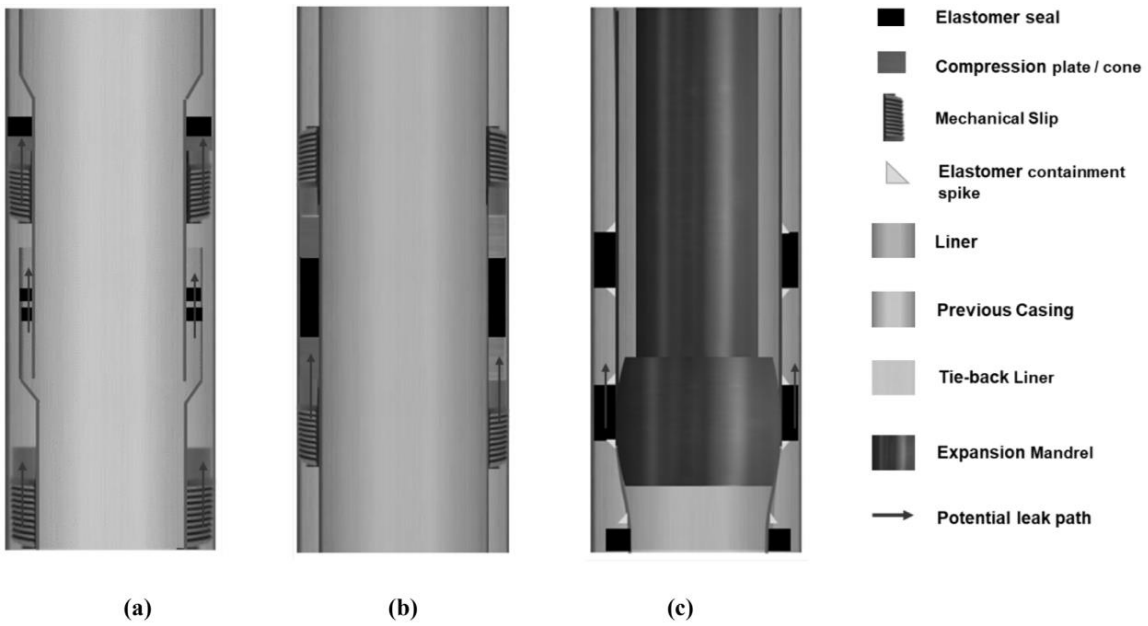

Figure 2. Differences among (a) liner top packer assembly, (b) integral liner hanger seal, (c) expandable liner hanger seal assembly.

An expanded liner hanger represents a relatively recent technological development. It comprises an elastomeric element mounted on the outer surface of a smooth liner body that contains no movable components (Fig. 2c). The operating principle involves running a solid mandrel with an outer diameter larger than the inner diameter of the liner hanger, thereby expanding the liner either mechanically or hydraulically. As the liner body enlarges, the elastomer elements are compressed against the casing wall, activating and energizing the sealing mechanism. These seals not only provide hydraulic isolation but also function as structural anchors for the liner.

At the wellhead, a slip-and-seal type casing-hanger assembly is commonly used [7]. The activation method of a conventional liner hanger seal assembly closely resembles that of the slip-and-seal assembly (Fig. 3). During activation, axial force is transmitted to the elastomer component, causing it to deform radially and create a pressure-tight seal that isolates the annular pressure beneath the hanger from the wellbore.

In offshore jack-up drilling operations with mudline completions, a mechanically set seal assembly is often utilized. In this system, cap screws are manually tightened against the compression plate using a wrench, which in turn compresses the elastomer element and establishes the seal.

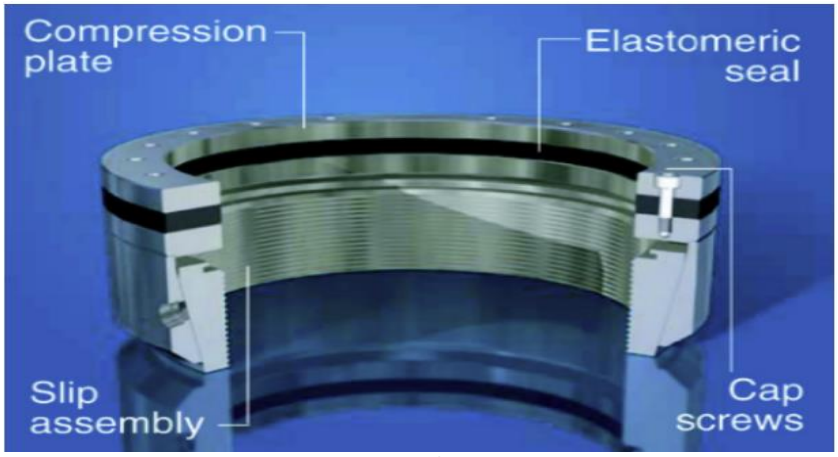

Figure 3. Mechanical set of slip and seal assembly.

Packer equipment is commonly employed to isolate annular spaces between the production tubing and casing or to separate different production zones within a well. Similar to casing and liner hanger systems, packers utilize a cone and slip mechanism to apply either mechanical or hydraulic compression to the elastomer element, thereby activating the seal (Fig. 4a) [8].

Recent advancements in technology have introduced packer systems that use elastomer materials capable of swelling when exposed to oil-based fluids. Upon contact, the elastomer expands radially, allowing the sealing element to press firmly against the opposing surface and establish isolation.

In situations involving loss of well control, such as formation kicks or blowouts, the blowout preventer (BOP) serves as a vital component of wellhead safety equipment. Acting as a secondary barrier or fail-safe mechanism, the BOP typically contains a solid, donut-shaped elastomer element (Fig. 4b). When hydraulic pressure is applied during a potential kick event, the elastomeric donut deforms tightly around the drill pipe, effectively sealing the wellbore. The elastomer remains in sustained contact with the pressure exerted by the formation fluids, maintaining well control and preventing uncontrolled flow.

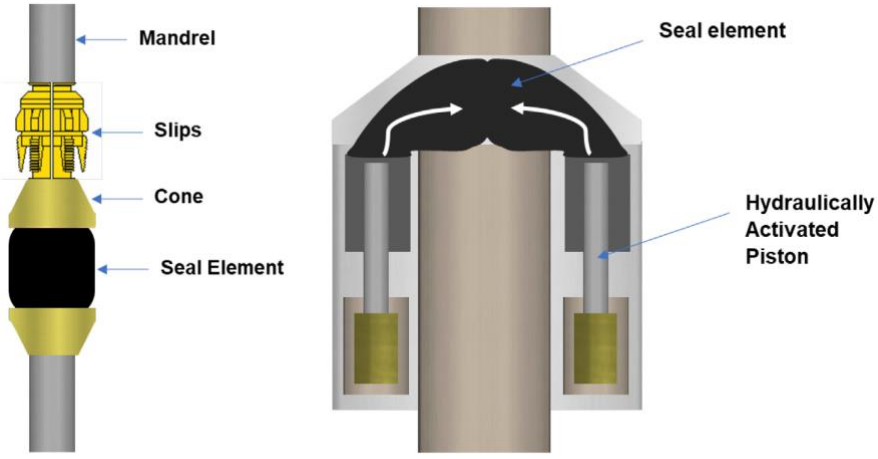

Figure 4. Elastomer seal components (black color) in (a) packer, (b) blowout preventor after closure.

4. Failure in Seal Assembly

Seal assembly failures often lead to expensive repair operations, increasing the overall cost of well construction and maintenance while also disrupting company activities. If such failures go undetected for an extended period, they can critically compromise well integrity and potentially cause a loss of well control, posing severe risks to human health, safety, and the environment.

The SINTEF organization maintains a comprehensive historical database documenting incidents of well blowouts and loss of well control (LOWC). According to SINTEF records, most blowouts occur during drilling operations, followed by incidents during workover, completion, and production stages. Several studies have performed statistical analyses of SINTEF's data to estimate how frequently seal-related factors contribute to these incidents.

Figure 5 illustrates the distribution of causes for all LOWC events recorded between 1980-1994 and 2000-2015. The sections of the pie charts shown in black and gray represent incidents associated with failures of subsurface safety valves, leaks in wellhead components, Christmas tree assemblies, or blowout preventers (BOPs) following seal malfunction. The data clearly indicate that approximately 46% of all secondary barrier failures are attributable to equipment containing elastomeric seals.

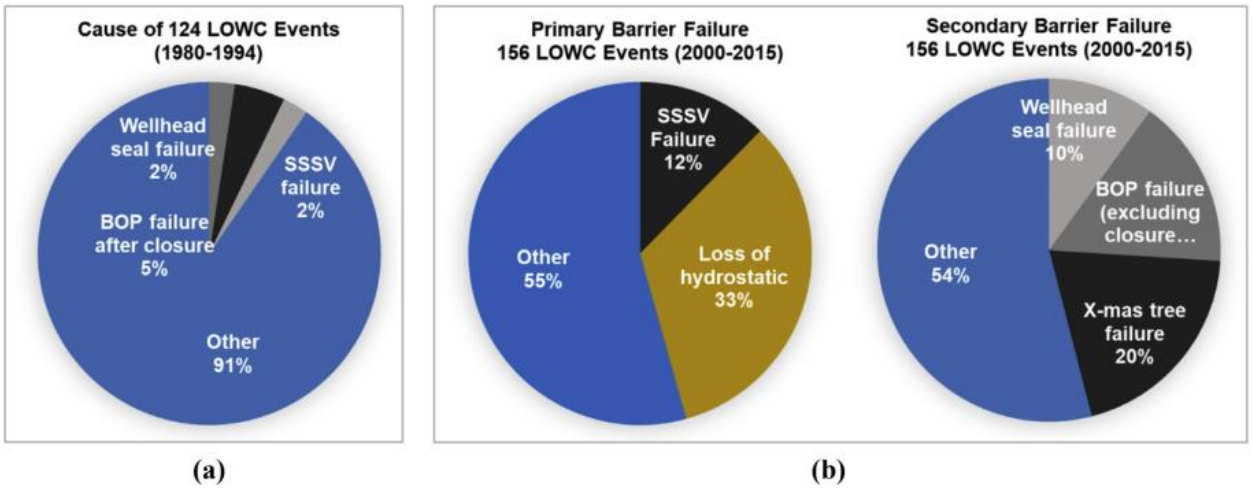

Figure 5. Causes of LOWC events occurred during (a) 1980-1994, and (b) 2000-2015. Black and grey shades represent causes most likely related to sealing.

5. Failure Mechanisms in Elastomer Seals

Elastomer seals are prone to several types of failure mechanisms during their lifecycle, including abrasion and wear (Fig. 6b). Such failures may occur during storage, handling, or installation. The primary causes typically include insufficient lubrication, uneven or rough contact surfaces, and the presence of foreign particles or debris at the sealing interface [9].

Thermal degradation of elastomers at elevated temperatures is another common failure mode. Under extreme temperature variations, elastomer seals may develop radial cracks or display signs of material softening and embrittlement. Generally, elastomeric materials struggle to maintain effective sealing performance at temperatures exceeding 250-300° F.

Mechanical failures such as extrusion and nibbling (Fig. 6d) also significantly reduce sealing efficiency. This issue arises when an elastomer element is exposed to frictional forces on moving surfaces or to cyclic/static loads that induce repeated stress. Over time, the seal material can be pulled, torn, or gradually eroded, leading to material loss. Additionally, shear damage may occur when part of the seal is forced into an extrusion gap. Such extrusion failures not only impair the sealing capability but can also hinder the retrieval of service tools or equipment from the well.

Compression set failure (Fig. 6e) is another degradation mode characterized by permanent deformation of the seal. The most frequent cause is improper seal dimensioning, which can lead to early extrusion or loss of sealing contact pressure.

Among all failure types observed in oil and gas applications, chemical degradation (Fig. 6f) is particularly common. During operation, elastomers are exposed to a variety of chemically aggressive substances, including drilling, completion, and fracturing fluids, as well as formation brines and production fluids containing acids, caustics, solvents, and other corrosive components. These chemicals can diffuse into the elastomer matrix, deteriorating the polymer structure. Elevated temperatures accelerate this process, worsening the chemical attack. Fluid absorption can also cause volumetric swelling of the elastomer, increasing its susceptibility to abrasion and extrusion failures.

Furthermore, contact with oxidizing agents such as ozone during storage, transportation, or service can initiate chain scission reactions within the polymer network. This process weakens the molecular bonds and accelerates material degradation, particularly at higher operating temperatures.
Fernández and Castaño (2016) investigated the effects of crude oil exposure on elastomers over 168 hours at 150° F and 1000 psi. Their results showed that aging led to reduced tensile strength and elongation at break, increased volumetric swelling, and decreased hardness and compression set resistance. The deterioration was more severe when the crude oil contained higher concentrations of saturates and aromatics.

Common gases found in oil and gas wells hydrogen sulfide (H_2S), carbon dioxide (CO_2), and methane (CH_4) can also affect elastomer performance. CO_2 and H_2S are particularly aggressive, causing chemical degradation of elastomeric materials. Although CH_4 does not typically react chemically with elastomers, it can penetrate the polymer structure and induce physical changes such as swelling or blistering, further compromising sealing integrity.

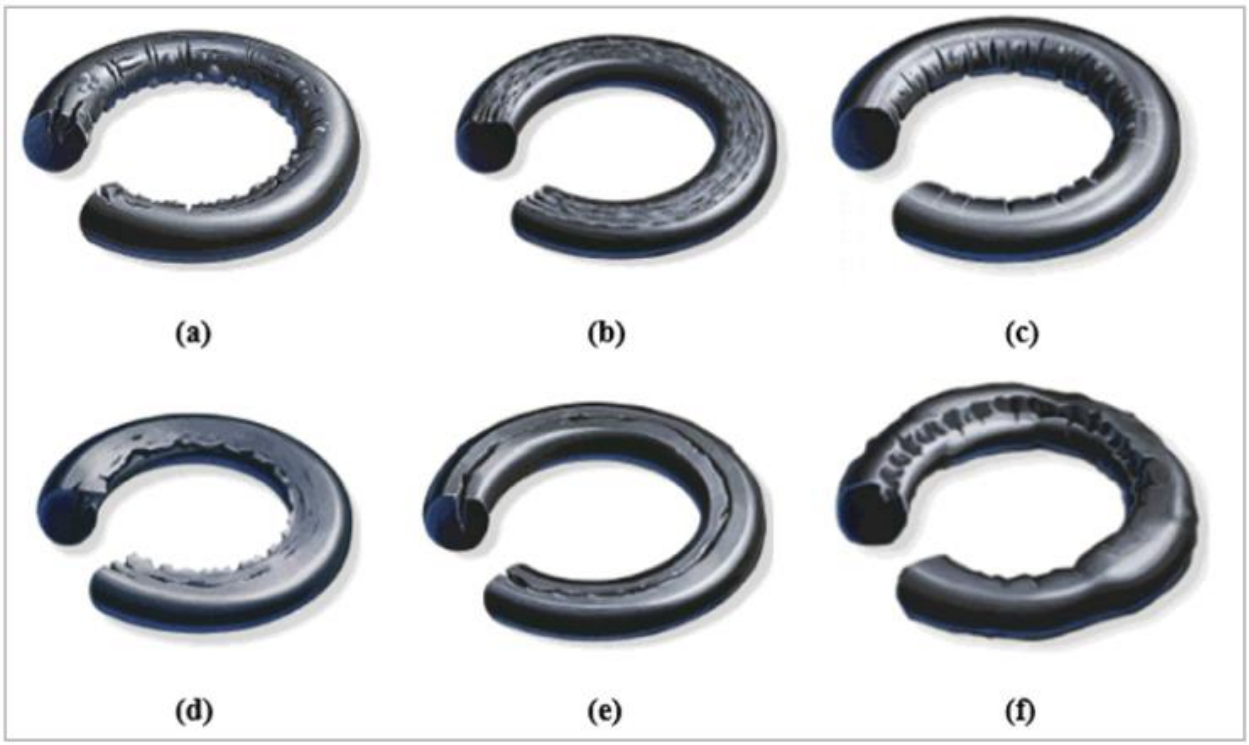

Figure 6. Failures in elastomer O-ring: (a) explosive decompression, (b) abrasion friction, (c) thermal degradation, (d) extrusion, (e) compression set, (f) chemical degradation.

6. Evaluation of Seal Performance

A comprehensive understanding of both elastomer material properties and seal assembly design is essential for accurately assessing sealing performance. The mechanical characteristics of the elastomer determine how the material deforms under load, which in turn influences its ability to maintain an effective seal. In oil and gas applications, elastomer seal components are generally stiffer and often assumed to exhibit linear elastic behavior. Under this assumption, only the elastic modulus and Poisson's ratio are typically required to describe material behavior [10].

However, at higher stress levels, elastomers display hyperelastic characteristics, meaning that their loading and unloading responses differ and depend on factors such as time, frequency, and dynamic load conditions. To model this nonlinear behavior accurately, constitutive models such as Neo-Hookean, Mooney-Rivlin, Ogden, and Yeoh are commonly employed. Experimental testing, such as uniaxial, planar, and biaxial tension tests, as well as volumetric compression tests, is necessary to define the parameters for these hyperelastic models.

To evaluate the suitability of an elastomer seal, a variety of material tests are typically conducted. The selection of test parameters depends on the manufacturer, researcher, and specific application. Commonly measured properties include curing characteristics, hardness, elongation at break, tensile and elastic moduli, torsional modulus, compression set, compression stress relaxation, rapid gas decompression (RGD) resistance, fluid compatibility, permeability, tear and abrasion resistance, and extrusion resistance. Most studies to date have focused on laboratory-scale testing of these fundamental material properties.

However, relatively few investigations have explored how these material properties influence seal assembly performance, particularly in terms of the contact stress generated at the sealing interface. One such study examined the effect of elastomer composition on the sealing behavior of compression packers. Three hydrogenated nitrile butadiene rubber (HNBR) formulations with different carbon black contents were tested. The authors measured uniaxial stress and compression behavior and implemented nonlinear constitutive models in a three-dimensional finite element analysis (FEA). Results indicated that sealing performance increased approximately linearly with applied setting pressure (Fig. 7). Nonetheless, no direct experimental or analytical data on contact stress were reported.

In the same study, the three elastomers were ranked based on structural stress levels in the supporting components and the likelihood of shoulder extrusion. The experimentally obtained extrusion–pressure curves showed strong agreement with theoretical model predictions.

Further research investigated extrusion behavior in commonly used oilfield elastomers through both experimental and FEA approaches. The study examined how differential pressure influenced extrusion in O-ring samples, identifying spiral failure due to extrusion as a primary failure mode under high-pressure, high-temperature (HPHT) conditions. The results demonstrated that the critical tear pressure, which is temperature-dependent, had a significant effect on seal material performance. The authors emphasized the importance of employing FEA not only for O-ring analysis but also for extending testing to full assembly-level seal design.

Additional investigations analyzed the effect of various design parameters on the sealing efficiency of elastomers used in conventional liner hanger assemblies. Parametric studies using validated 3D FEA models revealed that both Poisson's ratio and elastic modulus have a pronounced influence on the resulting contact stress (Fig. 8). The findings highlighted the necessity of using accurate material property data in seal design to avoid significant overestimation or underestimation of sealing performance.

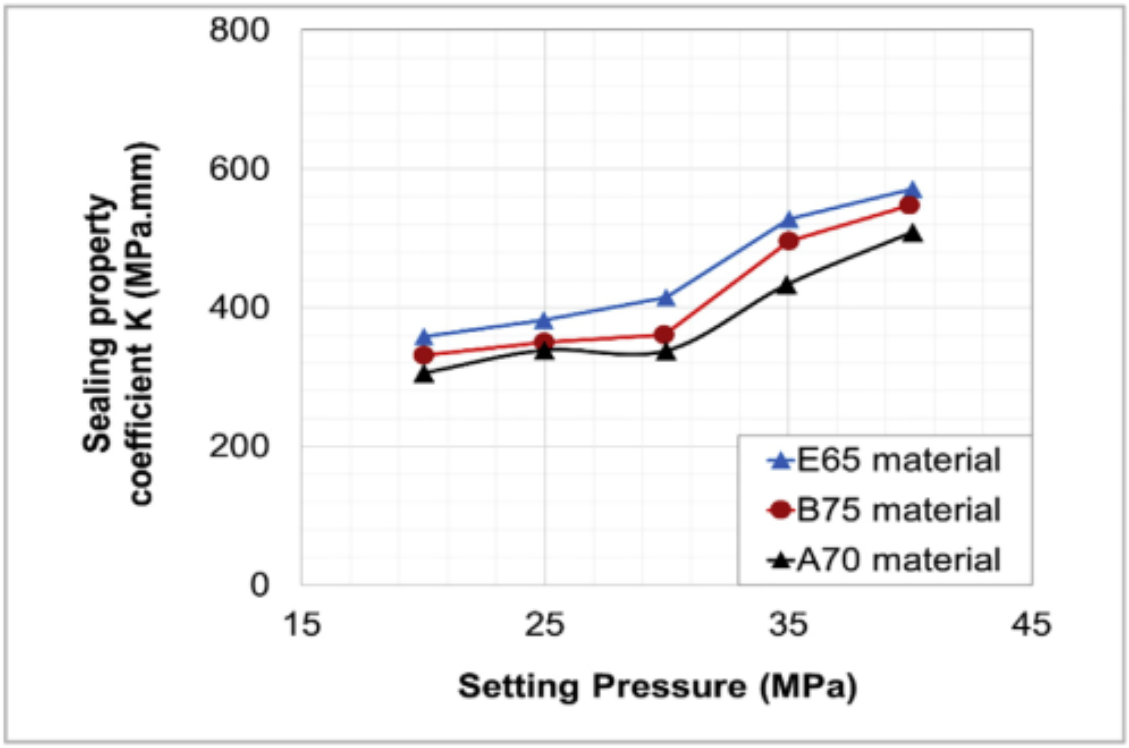

Figure 7. Sealing performance of the elastomer packer element as a function of setting pressure.

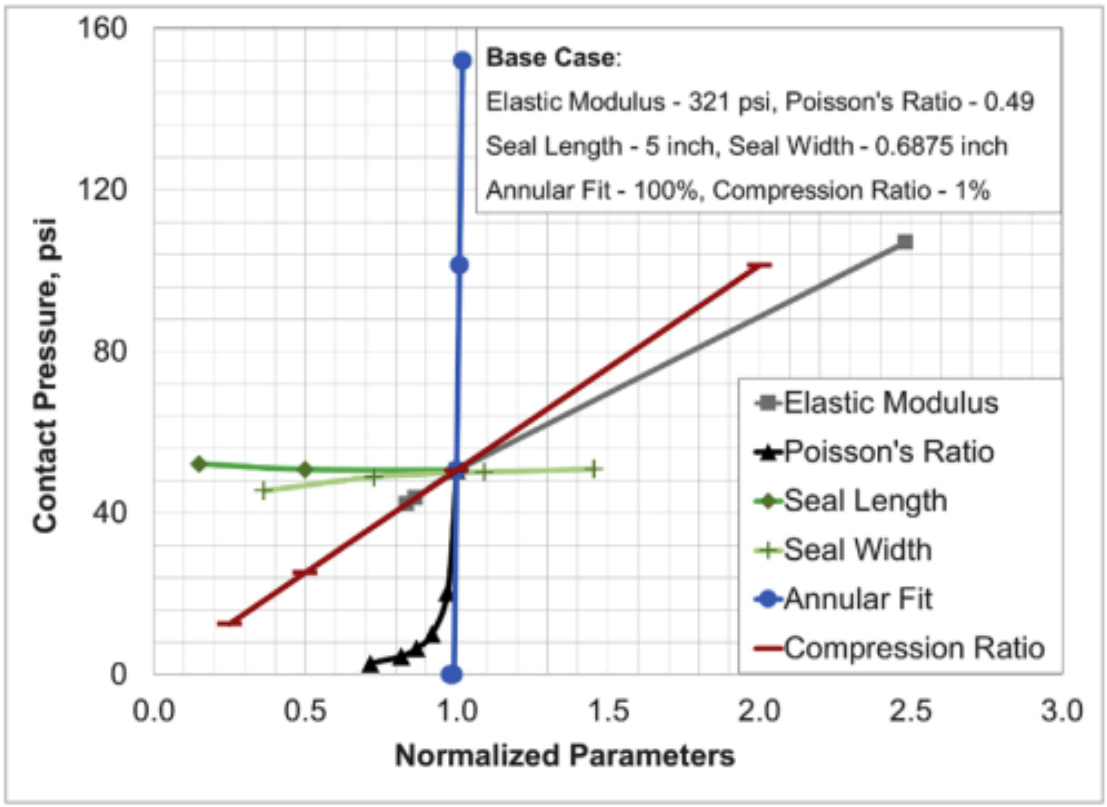

Figure 8. Sensitivity of contact pressure to various parameters.

7. Research Gaps and Future Directions

The industry has explored alternatives such as metal-to-metal (M2M) seals, particularly for applications involving harsh chemical environments, high pressures, and elevated temperatures. Metal seals offer several advantages, including superior resistance to extreme temperatures, pressures, and chemical attack, robust mechanical properties, minimal porosity, and extended shelf life. However, a key limitation of metal seals is their lack of flexibility and elasticity. To address this, researchers are developing innovative designs, such as lattice seals that combine a metallic structure with a thermoplastic matrix. Despite these advancements, these newer seal concepts remain under development.

Other challenges associated with metal seals include higher costs and a limited selection of material grades. Unlike elastomeric seals, the performance of metal seals is highly sensitive to the surface characteristics of the metal components. A microscopic-level modeling approach has been proposed to predict how surface roughness impacts sealability. By accounting for surface properties, the model can estimate contact stresses and corresponding leakage rates. The study concluded that surface finish, typically quantified as a root mean square (RMS) value, is the primary factor controlling leakage in M2M seals. Surfaces with randomly distributed roughness, such as those from casting, require higher contact stresses to achieve zero leakage compared to surfaces with more uniform asperity distributions, like machined components. Further research is needed to determine realistic leakage tolerances for metallic seals.

Additional challenges for metal seals include dynamic sealing performance and reduced effectiveness in the presence of particulate debris. Overall, due to these limitations, metal seals currently have narrower applicability compared to elastomer seals. Elastomers remain the preferred sealing material because of their low cost, durability, and ability to seal against irregular and dynamic surfaces.

8. Results

1. Analysis of historical well control incidents indicates that 46% of secondary barrier failures were attributable to seal equipment. In contrast to studies on material failure mechanisms, there is limited research examining the failure of functional seal assemblies and their impact on well control.
2. The performance of a seal assembly is influenced not only by elastomer material properties but also by factors such as seal geometry, the energization method, design of housing and support components, operational loads, contact interface conditions, and, in some cases, geomechanical considerations.
3. Existing industry standards primarily emphasize laboratory testing of standardized material samples. There are currently no guidelines for the design of elastomer seals at the full equipment level. Standards for material selection should be adapted to the specific application, seal type, and size of the equipment.
4. Future research should focus on seal assembly design, in addition to material characterization, to enhance elastomer reliability. There is a pressing need for robust methodologies that allow scaling laboratory findings to field-scale applications with extended service life. Developing a comprehensive database of elastomer material properties under high-pressure, high-temperature (HPHT) conditions would also provide significant support to the industry.

Author Contributions

The authors collaboratively designed the study, carried out the analysis, and contributed to writing and revising the manuscript. Both authors approved the final version.

Conflict of Interest

The authors declare no conflicts of interest.

Funding

This research was not supported by external funding.

Acknowledgment

The authors are deeply grateful to Dr. Durdana Rustamova for her continuous guidance, constructive feedback, and encouragement.

Data Availability Statement

As a review article, this study did not generate any new primary data, code, or experimental results. All findings, conclusions, and data discussed herein are derived exclusively from previously published and publicly available scientific literature, which are fully cited in the References section.

Abbreviations

High-Pressure High-Temperature (HPHT), Bureau of Safety and Environmental Enforcement (BSEE), Subsurface Safety Valves (SSSVs), Blowout Preventer (BOP), Loss of Well Control (LOWC), Selskapet for Industriell og Teknisk Forskning (SINTEF), Hydrogen Sulfide (H_2S), Carbon Dioxide (CO_2), Methane (CH_4), Rapid Gas Decompression (RGD), Hydrogenated Nitrile Butadiene Rubber (HNBR), Finite Element Analysis (FEA), Metal-to-metal (M2M).

References

1. Patel, H., Salehi, S., Ahmed, R., & Teodoriu, C. (2019). Review of elastomer seal assemblies in oil & gas wells: Performance evaluation, failure mechanisms, and gaps in industry standards. *Journal of Petroleum Science and Engineering*, *179*, 1046-1062. https://doi.org/10.1016/j.petrol.2018.12.051
2. Akhtar, M., Qamar, S. Z., & Pervez, T. (2012). Swelling elastomer applications in oil and gas industry. *J. Trends Dev. Mach. Assoc. Technol*, *16*(1), 71-74.
3. Shavandi, M., & Tang, F. (2017, July). Load Monitoring and Condition Assessment of High-Pressure-High-Temperature (HPHT) Subsea Facilities. In *Pressure Vessels and Piping Conference* (Vol. 57984, p. V005T05A006). American Society of Mechanical Engineers. https://doi.org/10.1115/pvp2017-66243
4. Akhtar, M., Qamar, S. Z., Pervez, T., & Al-Jahwari, F. K. (2018). Performance evaluation of swelling elastomer seals. *Journal of Petroleum Science and Engineering*, *165*, 127-135. https://doi.org/10.1016/j.petrol.2018.01.064
5. Wang, Z., & Wang, T. (2019). A review on the deformation and failure of seals in oilfield. *Chinese Journal of Theoretical and Applied Mechanics*, *51*(3), 635-655.
6. Chen, N., Dong, X., & Ma, Y. (2022). Evaluation on the Seal Performance of SMP-Based Packers in Oil Wells. *Polymers*, *14*(4), 836. https://doi.org/10.3390/polym14040836
7. Al-Kharusi, M. S., Qamar, S. Z., Pervez, T., & Akhtar, M. (2011, May). Non-linear model for evaluation of elastomer seals subjected to differential pressure. In *SPE Kingdom of Saudi Arabia Annual Technical Symposium and Exhibition* (pp. SPE-149032). SPE. https://doi.org/10.2118/149032-ms
8. Patel, H., & Salehi, S. (2019). Investigation of elastomer seal energization: Implications for conventional and expandable hanger assembly. *Energies*, *12*(4), 763. https://doi.org/10.3390/en12040763
9. Qamar, S. Z., Pervez, T., & Akhtar, M. (2016). Performance evaluation of water-swelling and oil-swelling elastomers. *Journal of Elastomers & Plastics*, *48*(6), 535-545. https://doi.org/10.1177/0095244315611169
10. Mody, R., Gerrard, D., & Goodson, J. (2013). Elastomers in the oil field. *Rubber Chemistry and Technology*, *86*(3), 449-469. https://doi.org/10.5254/rct.13.86999

Review Article

Quantum Effects at the Nanoscale: A Comparative Study of Jaynes-Cummings-Hubbard and Bose-Hubbard Models

Narmin A. Azizli[1] **and Mubariz B. Huseynzada**[2]

[1, 2]Department of Mechanics and Mathematics, School of Advanced Technologies and Innovation Engineering, Western Caspian University, 17A Ahmad Rajabli Street, III Parallel, AZ1001 Baku, Azerbaijan

Received: 06.11.2025 Accepted: 17.11.2025 Published: 19.11.2025

https://doi.org/10.54414/OTDJ9129

Abstract

As the characteristic dimensions of a physical system shrink to the nanometer scale, its behavior is governed primarily by quantum mechanics rather than by classical laws. In this regime, effects such as barrier tunnelling, energy quantization, and quantum coherence play a central role in how nanoscale devices function. These phenomena are particularly prominent in platforms such as graphene and semiconductor quantum dots, where they have a pronounced impact on transport properties, optical behavior, and overall device performance. In parallel, lattice-based many-body models offer a concise theoretical framework for describing collective quantum states in engineered structures. The present work provides a conceptually oriented survey that links quantum phenomena at the nanoscale to two benchmark lattice Hamiltonians, namely the Jaynes-Cummings-Hubbard (JCH) and Bose-Hubbard (BH) models. The approach is qualitative and literature-based: results from quantum optics, cold-atom physics, and condensed-matter research are combined to interpret how the parameters of these models relate to experimentally tunable quantities, such as coupling strengths, confinement scales, and interaction energies. The main outcome of the review is threefold. First, tunnelling, graphene, and quantum dots can be viewed as natural settings where effective Hubbard-type descriptions arise. Second, despite describing different degrees of freedom-hybrid light-matter polaritons in the JCH case and interacting bosons in the BH case, both models display analogous phase structures with insulating and superfluid-like regimes. Third, reliable implementation of these phases in nanotechnological devices requires a careful mapping between abstract Hamiltonian parameters and specific design variables. The discussion indicates that JCH- and BH-type models should be regarded not only as abstract theoretical constructs but also as practical tools for guiding the design of future quantum technologies. Extensions to driven-dissipative dynamics and topological band structures are identified as promising directions for next-generation quantum simulators and nanoscale sensors.

Keywords: quantum tunnelling, graphene, quantum dots, Jaynes-Cummings-Hubbard model, Bose-Hubbard model, quantum simulators

1. Introduction

Nanotechnology deals with the control and manipulation of matter at length scales where the behavior of individual atoms and molecules becomes relevant. At these dimensions, the usual classical approximation breaks down, and features such as superposition, quantized energy spectra, and interference must be explicitly included in the description. As a consequence, the behavior of nanostructures is governed by quantum mechanics, and quantum effects turn from subtle corrections into dominant features of device operation.

Several quantum phenomena are particularly relevant for engineering at the nanoscale. Quantum tunnelling allows particles to traverse potential barriers that would be impenetrable in a classical picture. Confinement gives rise to discrete spectra and size-dependent optical properties. Long-lived coherence enables interference and entanglement between spatially separated degrees of freedom. These effects play central roles in

systems such as graphene-based conductors, tunnelling devices, and semiconductor quantum dots, which already underpin parts of modern electronics, photonics, and quantum information technology.

In parallel with advances in materials and fabrication, theoretical physics has produced a family of relatively simple but powerful lattice models that describe interacting quantum particles or quasiparticles. Among these, two frameworks are especially important for the present discussion. The Jaynes-Cummings-Hubbard (JCH) model extends cavity quantum electrodynamics to arrays of coupled light-matter sites, while the Bose-Hubbard (BH) model captures the competition between tunnelling and on-site interactions for bosons on a lattice. Both have been realized experimentally, for example, in cold-atom optical lattices and in photonic or superconducting circuits.

2. Quantum tunnelling

In quantum theory, a particle can still be detected on the far side of an energy barrier that would completely block it in classical mechanics; this counterintuitive process is known as quantum tunnelling. In the semiclassical (WKB) approximation, the tunnelling probability P through a one-dimensional barrier between the classical turning points x_1 and x_2 can be expressed as

$$P \propto \exp\left(-2\int_{x_1}^{x_2}\sqrt{\frac{2m}{\hbar^2}}[V(x)-E]\,dx\right) \quad (1)$$

where m is the particle mass, E is its energy, and V(x) denotes the potential profile. The exponential dependence on barrier width and height explains why tunnelling effects become prominent when characteristic dimensions approach the nanometer scale. Scanning tunnelling microscopy (STM) is a key technological application of this principle, exploiting electron tunnelling between a sharp tip and a sample surface to probe topography and local electronic structure with atomic resolution.

3. Graphene

Graphene is formed by a single sheet of carbon atoms organised in a two-dimensional honeycomb lattice. Owing to the symmetry of this lattice, the electronic band structure exhibits touching points between the valence and conduction bands, the so-called Dirac points, at which low-energy charge carriers behave effectively as massless fermions. As a result, charge carriers in graphene can move over micrometer distances with very little scattering, and the material exhibits high mobility and unconventional quantum Hall effects. Quantum phenomena such as Klein-type tunnelling through electrostatic barriers and robust coherence make graphene attractive for high-frequency electronics, precision metrology, and hybrid superconducting–graphene devices. Patterning graphene into nanoribbons or quantum dot structures further enhances confinement and makes it possible to approximate lattice models with tunable hopping and interaction parameters.

4. Quantum dots

Semiconductor quantum dots are nanoscale structures in which electrons and holes experience confinement along all three spatial directions. Confinement energies become comparable to or larger than thermal energy, so the system exhibits discrete energy levels reminiscent of atomic spectra. By adjusting dot size, composition, or shape during fabrication, one can shift level spacings and thus tune optical emission and absorption over a wide range. Quantum dots are exploited in light-emitting devices, display technologies, biological imaging, high-efficiency solar cells, and as single-photon sources. When coupled to optical cavities or waveguides, quantum-dot excitons can interact strongly with confined modes, forming polaritons that fit naturally within JCH-type descriptions. In arrays of coupled dots, the collective dynamics can emulate either Bose-Hubbard or Fermi-Hubbard physics, depending on the carriers and interactions involved.

5. Jaynes-Cummings-Hubbard model

In the Jaynes-Cummings description, a single two-level emitter (for example, an atom or qubit) exchanges excitations coherently with one quantized mode of the electromagnetic field confined in a cavity. Within the rotating-wave approximation, the corresponding Hamiltonian takes the form

$$H_{JC} = \hbar\omega a^{\dagger}a + \frac{1}{2}\hbar\omega_0\sigma_z + \hbar g(a\sigma_+ + a^{\dagger}\sigma_-) \quad (2)$$

where ω_C is the cavity frequency, ω_0 is the transition frequency of the two-level system, g is the light-matter coupling strength, $a^{\dagger}a$ are photon creation and annihilation operators, and $\sigma_z\sigma_{\pm}\sigma_-$ are Pauli operators acting on the two-level system. This model captures key features of cavity quantum electrodynamics, including coherent Rabi oscillations and vacuum Rabi splitting.

The Jaynes-Cummings-Hubbard model takes the single-cavity Jaynes-Cummings setting and replicates it across many sites, allowing photons to tunnel between neighbouring cavities while each two-level system interacts only with its local field mode. A commonly used form of the JCH Hamiltonian is:

$$\hat{H}_{JCH}=\sum_i(\hbar\omega_C\, a^{\dagger}{}_i a_i + \frac{\hbar\omega_0}{2}\,\sigma_i{}^z + \hbar g(a^{\dagger}\sigma_i{}^- + a\sigma_i{}^+)) - J\sum_{(I,j)} a_i^{\dagger}a_j \quad (3)$$

where J is the photon hopping amplitude between nearest-neighbor sites (i, j). The elementary excitations are hybrid light-matter polaritons whose spatial behavior depends on the balance between on-site interaction effects and inter-site tunnelling.

6. Bose-Hubbard model

The Bose-Hubbard framework describes bosonic particles residing on a lattice of discrete sites, where they are subject to local interactions and are able to tunnel between neighboring positions. One commonly employed form of the Bose–Hubbard Hamiltonian can be written as follows:

$$\hat{H}_{BH}= -J\sum_{(I,j)}(b_i^{\dagger}b_j + b_j^{\dagger}b_i) + \frac{U}{2}\sum_i n_i(n_i - 1) - \mu\sum_i n_i \quad (4)$$

Where $b_i^{\dagger}$ and b_I create and annihilate bosons at site i, $n_i = b_i^{\dagger}b_i$ is the number operator, J is the hopping amplitude, U is the on-site interaction strength, and μ is the chemical potential. Within the Bose-Hubbard description, bosons are allowed to hop from site to site while simultaneously feeling a repulsive cost when several particles accumulate on the same site. The competition between J and U gives rise to distinct phases, including Mott-insulating states and superfluid states.

This article aims to assemble these ingredients into a coherent picture: to show how basic quantum effects at the nanoscale and material platforms such as graphene and quantum dots can be understood in relation to JCH- and BH-type Hamiltonians, and how this viewpoint may assist the design of future quantum devices.

7. Materials and Methods

The study is organised as a narrative, theory-focused review rather than an original experimental investigation. It does not report new experimental measurements or simulations; instead, it synthesizes and organizes existing results from the literature. The methodological steps are as follows:

1. Studies on tunnelling, confinement, and coherence at the nanoscale are used to illustrate generic quantum effects relevant for device operation.
2. Experimental and theoretical work on graphene and semiconductor quantum dots is reviewed to identify how their properties can be described using effective lattice models.
3. Key parameters of the JCH and BH Hamiltonians, such as coupling strengths, detuning, hopping amplitudes, and interaction energies, are related qualitatively to experimentally tunable quantities in nanostructures, including geometry, material composition, cavity design, and external fields.
4. Parameter regimes associated with insulating versus superfluid-like phases are discussed in terms of how they might be approached in realistic nanotechnological platforms.

Because the goal is conceptual clarity rather than quantitative benchmarking, results are presented descriptively, with representative examples drawn from published work rather than from new datasets.

8. Results

The literature-based analysis allows several concise results to be formulated concerning the relationship between nanoscale quantum phenomena and lattice model descriptions.

First, tunnelling, confinement, and coherence emerge as common threads linking different nanoscale systems. Graphene, quantum dots, and related structures provide concrete environments in which these phenomena strongly influence electronic and optical behavior. In each case, the relevant quantum states can be viewed as occupying effective “sites” with well-defined energies and couplings, making the use of JCH or BH-type Hamiltonians natural.

Second, the Jaynes-Cummings-Hubbard and Bose-Hubbard models, although they act on different degrees of freedom, display structurally similar Hamiltonians and phase diagrams. Both incorporate local interaction terms and inter-site tunnelling, and both support regimes analogous to Mott insulators and superfluids. In JCH systems, the excitations are polaritons formed from light and matter; in BH systems, they are bosons such as atoms or exciton-polaritons. This structural similarity means that analytical and numerical methods developed for one model can often be adapted to the other.

Third, the correspondence between model parameters and experimental control knobs can be described systematically. In optical lattice experiments, laser intensities and magnetic fields fix tunnelling rates and interaction strengths. In cavity and circuit QED realizations, resonator geometry, detuning, and coupling strengths play a similar role. In graphene-based and quantum-dot devices, lithographic patterning, gate voltages, and material composition govern level spacing, overlap integrals, and interaction energies. These relationships demonstrate that the abstract parameter space of JCH and BH models can be mapped onto a space of practical design choices in nanotechnology.

9. Discussion

The results indicate that lattice models traditionally associated with cold-atom and quantum-optics experiments can also be interpreted from a nanotechnology perspective. Thinking in terms of JCH and BH Hamiltonians encourages a shift from viewing nanostructures as isolated components toward seeing them as parts of larger, interacting networks of quantum degrees of freedom. This is particularly relevant for quantum simulators, where the goal is to emulate complex many-body behavior in a controllable device.

Another implication is methodological. Because the JCH and BH models share a common structure, theoretical advances in one area can inform progress in the other. For example, techniques used to study the superfluid–Mott-insulator transition in BH systems can be adapted to explore polaritonic phase transitions in JCH

arrays. Conversely, progress in engineering strong light-matter coupling in cavity and circuit QED systems suggests strategies for enhancing effective interactions in solid-state nanodevices based on quantum dots or two-dimensional materials.

Realistic nanostructures, however, are subject to losses, disorder, and environmental noise. This motivates extending both models to open quantum systems where dissipation and external driving are treated explicitly.

Driven-dissipative analogues of JCH and BH Hamiltonians are already being explored theoretically and experimentally, and they are expected to be central for practical implementations of quantum simulators, sensors, and information-processing devices that must operate under non-ideal conditions.

10. Conclusion

Once device dimensions reach the nanometer regime, quantum effects cease to be small corrections and instead dominate the overall behavior of the system. Materials such as graphene and semiconductor quantum dots show how tunnelling, confinement, and coherence can be exploited to obtain novel transport and optical properties. At the same time, the Jaynes-Cummings-Hubbard and Bose-Hubbard models offer compact descriptions of interacting quantum excitations on lattices and provide a common language for discussing insulating and superfluid-like phases across different platforms.

By relating the parameters of these models to experimentally controllable quantities in real nanostructures, this review argues that JCH- and BH-type Hamiltonians can function as practical guides for the design of quantum devices. Ongoing advances in fabrication techniques, coherent-control methods, and theoretical modelling are expected to generalise these frameworks to more complex situations, such as driven–dissipative dynamics and topological band structures, further tightening the connection between many-body quantum theory and practical nanotechnological implementations.

Author Contributions

Both authors contributed equally to the conception, design, data analysis, and interpretation of the study. Both authors participated in drafting and revising the manuscript and approved the final version.

Funding

No funding was received for this research.

Conflicts of Interest

The authors declare that they have no conflicts of interest.

Acknowledgments

The authors would like to thank Dr. Durdana Rustamova for her valuable support and guidance during the preparation of this work.

Data Availability Statement

The data supporting the findings of this study are available within the article and its list of references. This article is a review based on previously published literature and does not report any new experimental data.

Abbreviations

Jaynes-Cummings-Hubbard (JCH), Bose-Hubbard (BH), Wentzel-Kramers-Brillouin (WKB), Scanning Tunnelling Microscopy (STM), Quantum Electrodynamics (QED).

References

1. Bera, D., Qian, L., Tseng, T. K., & Holloway, P. H. (2010). Quantum dots and their multimodal applications: a review. *Materials*, *3*(4), 2260-2345. https://doi.org/10.3390/ma3042260
2. Binnig, G., Rohrer, H., Gerber, C., & Weibel, E. (1982). Surface studies by scanning tunneling microscopy. *Physical review letters*, *49*(1), 57. https://doi.org/10.1103/physrevlett.49.57
3. Greentree, A. D., Tahan, C., Cole, J. H., & Hollenberg, L. C. (2006). Quantum phase transitions of light. *Nature Physics*, *2*(12), 856-861. https://doi.org/10.1038/nphys466
4. Greiner, M., Mandel, O., Esslinger, T., Hänsch, T. W., & Bloch, I. (2002). Quantum phase transition from a superfluid to a Mott insulator in a gas of ultracold atoms. *nature*, *415*(6867), 39-44. https://doi.org/10.1038/415039a
5. Hartmann, M. J., Brandao, F. G., & Plenio, M. B. (2006). Strongly interacting polaritons in coupled arrays of cavities. *Nature Physics*, *2*(12), 849-855. https://doi.org/10.1038/nphys462
6. Hensgens, T., Fujita, T., Janssen, L., Li, X., Van Diepen, C. J., Reichl, C., & Vandersypen, L. M. (2017). Quantum simulation of a Fermi–Hubbard model using a semiconductor quantum dot array. *Nature*, *548*(7665), 70-73. https://doi.org/10.1038/nature23022
7. Imamog, A., Awschalom, D. D., Burkard, G., DiVincenzo, D. P., Loss, D., Sherwin, M., & Small, A. (1999). Quantum information processing using quantum dot spins and cavity QED. *Physical review letters*, *83*(20), 4204. https://doi.org/10.1103/physrevlett.83.4204
8. Jaksch, D., Bruder, C., Cirac, J. I., Gardiner, C. W., & Zoller, P. (1998). Cold bosonic atoms in optical lattices. *Physical Review Letters*, *81*(15), 3108. https://doi.org/10.1103/physrevlett.81.3108
9. Michler, P., Imamoğlu, A., Mason, M. D., Carson, P. J., Strouse, G. F., & Buratto, S. K. (2000). Quantum correlation among photons from a single quantum dot at room temperature. *Nature*, *406*(6799), 968-970. https://doi.org/10.1038/35023100
10. Novoselov, K. S., Geim, A. K., Morozov, S. V., Jiang, D. E., Zhang, Y., Dubonos, S. V., & Firsov, A. A. (2004). Electric field effect in atomically thin carbon films. *science*, *306*(5696), 666-669. https://doi.org/10.1126/science.1102896
11. Wallraff, A., Schuster, D. I., Blais, A., Frunzio, L., Huang, R. S., Majer, J., & Schoelkopf, R. J. (2004). Strong coupling of a single photon to a superconducting qubit using circuit quantum electrodynamics. *Nature*, *431*(7005), 162-167. https://doi.org/10.1038/nature02851